Department of Physics and Astronomy
Heidelberg University

Bachelor Thesis in Physics
submitted by

Nele Marie Griesbach

born in Reutlingen (Germany)

2023

Characterization of a closed-loop noble gas recycling system for high-repetition rate high-harmonic generation

This Bachelor Thesis has been carried out by Nele Marie Griesbach at the
Max-Planck-Institut für Kernphysik in Heidelberg
under the supervision of
Apl. Prof. Dr. José R. Crespo López-Urrutia

Abstract

The use of noble gases is indispensable for producing an extreme ultraviolet frequency comb, using high-repetition rate high-harmonic generation. However, their high cost and limited availability have prompted the development of a closed-loop noble gas recycling system. In our system, the target gas is injected through a typically 20-100 µm sized nozzle into a laser focus, subsequently caught by vacuum pumps and compressed to a pressure of up to 200 bar. In this work, the leakage rates and recycling efficiency of the system are investigated, crucial parameters for the performance of the recycling system. The study aims to evaluate the effectiveness of the recycling system in maintaining gas purity and minimizing gas consumption, thereby significantly reducing operating costs. Consequently, enabling long extreme ultraviolet operation in the order of weeks, necessary for ultra-narrow bandwidth direct frequency comb spectroscopic needs, which would not be possible without a gas recycling system.

Zusammenfassung

Die Verwendung von Edelgasen ist für die Erzeugung eines extrem ultravioletten Frequenzkamms mittels der Generation von hohen Harmonischen bei hoher Wiederholrate unerlässlich. Die hohen Kosten und die begrenzte Verfügbarkeit von Edelgasen haben zur Entwicklung eines Edelgas-Recycling-Systems mit geschlossenem Kreislauf geführt. Bei diesem System wird das Zielgas durch eine typisch 20-100 µm große Düse in den Laserfokus injiziert, anschließend von Vakuumpumpen aufgefangen und auf einen Druck von bis zu 200 bar komprimiert. In dieser Arbeit werden die Leckraten und die Recyclingeffizienz des Systems untersucht, entscheidende Parameter für die Leistung des Recyclingsystems. Die Studie zielt darauf ab, die Effektivität des Recyclingsystems bei der Aufrechterhaltung der Gasreinheit und der Minimierung des Gasverbrauchs zu bewerten und dadurch die Betriebskosten erheblich zu senken. Dies ermöglicht einen langen Betrieb im extremen Ultraviolettbereich in der Größenordnung von Wochen, der für direkte Frequenzkamm-Spektroskopie mit extrem schmaler Bandbreite erforderlich ist und ohne ein Gasrecyclingsystem nicht möglich wäre.

Contents

1 Introduction **1**
- 1.1 XUV Spectroscopy . . . 1
- 1.2 Gas Recycling . . . 2

2 Theoretical Background **5**
- 2.1 High Harmonic Generation . . . 5
  - 2.1.1 Three-Step Model . . . 5
  - 2.1.2 Phase Matching of HHG . . . 6
  - 2.1.3 Steady-State Plasma . . . 10
  - 2.1.4 Pressure-induced Phase Matching . . . 11
- 2.2 Model Conceptions of Gases . . . 12
  - 2.2.1 Ideal Gas . . . 12
  - 2.2.2 Real Gas . . . 13
  - 2.2.3 Modeling Gas Leakage Rates . . . 14

3 Experimental Setup **17**
- 3.1 Femtosecond Enhancement Cavity . . . 17
  - 3.1.1 fsEC Setup . . . 18
  - 3.1.2 Gas Injection System . . . 19
- 3.2 Differential Pumping System . . . 20
- 3.3 Gas Recycling Setup . . . 22
  - 3.3.1 Low Pressure System . . . 25
  - 3.3.2 Compressor Station . . . 25
  - 3.3.3 High Pressure System . . . 26
  - 3.3.4 Components Used . . . 26

4 Analysis **31**
- 4.1 Leakage Characterization . . . 31
  - 4.1.1 Leakage Compressors . . . 31
  - 4.1.2 Leakage Diaphragm Pump . . . 35
- 4.2 Nozzle Consumption . . . 38
  - 4.2.1 Consumption for various Nozzle Sizes . . . 39
  - 4.2.2 Consumption for different Gases . . . 41
- 4.3 Gas Recycling . . . 43
  - 4.3.1 Recycling Argon at 55 bar . . . 43
  - 4.3.2 Recycling Krypton at 55 bar . . . 45
  - 4.3.3 Recycling Argon at 100 bar . . . 48

5 Conclusion and Outlook **51**

Acronyms **53**

Bibliography **55**

Acknowledgements **59**

1 Introduction

1.1 XUV Spectroscopy

The Standard Model of particle physics [1] describes fundamental interactions to an exceptional degree. Nonetheless, it cannot explain the imbalance between matter and antimatter [2], as well as the existence of dark matter [3] and dark energy [4]. Until now, the Standard Model cannot be unified with the theory of general relativity [5]. This provides strong motivation to search for physics beyond the Standard Model.

The high dimensionalities of string theory suggest that the fundamental constants vary in space and time [6], such as the proton-to-electron mass ratio $\mu = m_\mathrm{p}/m_\mathrm{e}$ and the fine structure constant $\alpha = e^2/(4\pi\varepsilon_0 hc)$, which describes the strength of the electromagnetic interaction. These fundamental parameters in atomic, molecular and optical physics can be measured by atomic clocks. Dirac's theory of the hydrogen atom shows that atoms are dependent on α, which enables atomic spectroscopy the detection of a possible variation in the fine structure constant α. For this reason, the search for atomic systems with the highest discrepancy on α dependency is of interest. Due to relativistic effects, the highly charged ions HCI sensitivity is expected to be two orders of magnitude higher compared to neutral or single charged atom systems. An optical atomic clock based on a HCI has recently been demonstrated by S. King *et al.* [7]. With many ultra-narrow transitions of HCI lying in the X-ray and extreme ultraviolet (XUV) region, a coherent light source in these specific regimes is necessary. One approach to achieve this is the upconversion of laser radiation from optical or near-infrared (NIR) wavelengths by high harmonic generation (HHG). This technique allows an XUV frequency comb to be produced by stabilizing the repetition rate and the carrier-envelope phase of the NIR comb, enabling direct frequency comb spectroscopy in the XUV regime [8–10].

In our laboratory, we aim to perform precision spectroscopy of HCI. For this purpose, HCI are produced in an electron beam ion trap (EBIT) [11] and sympathetically cooled in a superconducting Paul trap (CryPTex-SC) [12]. An XUV frequency comb, built by J. Nauta [8, 10], is required to enable XUV transition in HCIs. In this way, the HCI state can be read out using quantum logic spectroscopy [13]. An overview is shown in Fig. 1.1. The XUV frequency comb is based on the interaction of a high-intensity NIR frequency comb with a dense gas jet for the generation of phase-coherent high harmonics (HH) [14].

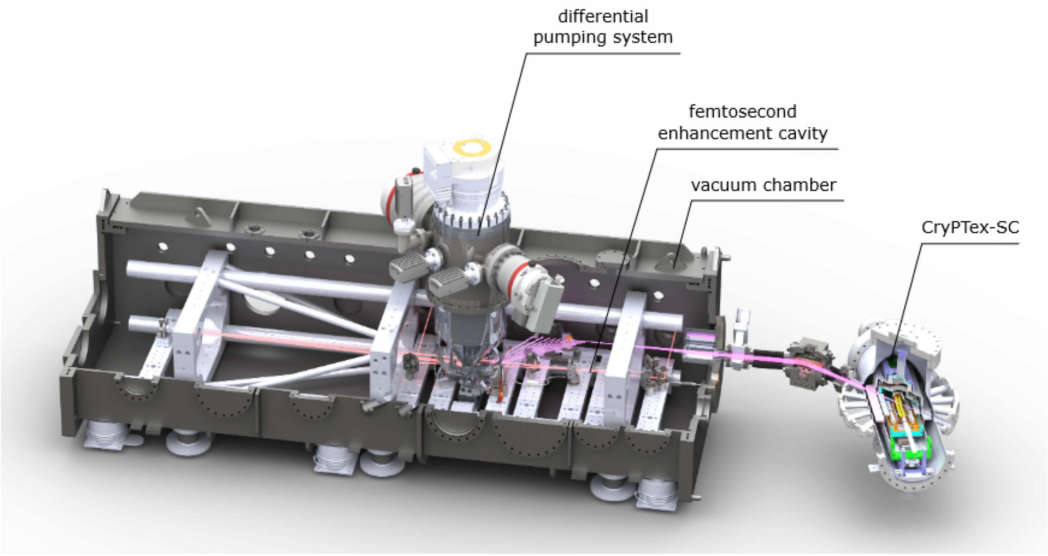

Figure 1.1: Schematic overview of the XUV frequency comb connected to CryPTex-SC for spectroscopy of HCIs. The pulses of the frequency comb are further amplified in an enhancement cavity to produce an XUV frequency comb.

1.2 Gas Recycling

The upconversion from NIR to XUV wavelengths via HHG is a well-established method for spectroscopy pump-probe and frequency measurements in the XUV regime. However, the process typically requires the use of noble gases such as xenon, neon, argon or krypton due to their high ionization potential. This can result in high costs and waste, particularly as the demand for noble gases in various industries continues to rise. In healthcare, noble gases are used in asthma treatments [15], anesthesia and as a contrast agent for medical imaging [16]. Argon is commonly used in welding and cutting processes to create an inert atmosphere that prevents oxidation and contamination of the metal being welded or cut [17]. Helium is used as a cooling agent in cryogenics, superconductivity, and nuclear magnetic resonance imaging due to its low boiling point and high thermal conductivity [18]. Noble gases also find applications in dark matter searches [19]. Furthermore, the availability of some noble gases such as xenon (abundancy of 0.09 ppb in the atmosphere [20]), is limited due to their rarity in the atmosphere.

Due to the higher demand and the resulting higher costs of noble gases, HHG operation necessitates a gas recycling system to enable a continuous supply of gas for spectroscopy needs. A few groups already implemented such systems for HHG [21, 22]. However, these systems have had limitations, such as a maximum pressure of 10 bar [21]

or an inability to operate in a continuous closed-loop [22]. To address these issues, we developed a closed-loop noble gas recycling system that enables continuous operation and compression of gas up to a pressure of 200 bar, which facilitates refilling of gas bottles and switching between gas species [23–25].

This work investigates the leakage rates of the system to determine the recycling rate of the closed-loop noble gas recycling system. In Chapter 2, the theoretical foundation required to understand the recycling system is discussed. Next, an overview of the experimental setup in Chapter 3 is provided. Chapter 4 focuses on the analysis of the system. Last, a summary and outlook in Chapter 5 is provided.

2 Theoretical Background

This Chapter focuses on covering the theoretical concepts needed in this thesis. First, a theoretical description of HHG is given. Second, plasma formation in gases is explained. Third, the thermodynamic processes of gases are discussed to understand the gas recycling process.

2.1 High Harmonic Generation

HHG is a highly nonlinear process in which photons of higher energy, the HH, are generated from low-energy photons of a driving laser. HH inherit properties such as temporal and spatial coherence, which makes it possible to generate laser light outside the commercially available range of far infrared (IR) to mid-ultraviolet (UV). Since the discovery of HHG, this has found many research applications, e.g., precision frequency metrology [26] and applied microscopy [27]. In our case, HHG is applied to perform laser spectroscopy of HCI. In HCIs, electrons are bound strongly to the nucleus due to the high proton excess. This shifts electronic transitions to the XUV region, which necessitates using HHG for spectroscopy. To get a complete picture of the HHG process, a quantum mechanical model, the Lewenstein model, is required [28]. Nevertheless, a semi-classical approach is sufficient in our case. This approach is also known as the three-step model [28, 29], which will be described in Subsection 2.1.1. Further, phase-matching conditions must be met between the driving laser and the harmonic laser field to make the HHG process as efficient as possible, which is sketched in Subsection 2.1.2.

2.1.1 Three-Step Model

The three-step model is illustrated in Fig. 2.1.

1. *Ionization*: When hitting a gas target, the oscillating laser field (red) distorts the Coulomb potential (blue) of the gas atoms such that the electron (green) can tunnel through the Coulomb barrier. The free electron has a cycle-averaged quiver energy, called ponderomotive energy

$$U_{\text{pond}} = \frac{e^2 \cdot I_{\text{peak}}}{2 \cdot c\varepsilon_0 m_e \omega_c^2}, \tag{2.1}$$

   where e is the elementary charge, I_{peak} the peak driving laser intensity, ε_0 the vacuum permittivity, ω_c the oscillating wave carrier frequency and electron mass m_e.

2. *Propagation*: The oscillating laser field accelerates the free electron, where the laser field is given by

$$E(t) = E_0 \cos(\omega t). \tag{2.2}$$

φ_i is the instantaneous phase of the laser field. After half a laser cycle, the sign of the electric field reverses, which leads to an acceleration of the electron back to the parent ion. The position x and velocity v of the free electron can be described by [30]

$$x(\varphi) = \frac{eE_0}{m_e\omega_c^2}(\cos(\varphi_i) - \cos(\varphi) + (\varphi - \varphi_i)\sin(\varphi_i)), \tag{2.3}$$

$$v(\varphi) = \frac{eE_0}{m_e\omega_c}(\sin(\varphi) - \sin(\varphi_i)). \tag{2.4}$$

For values of φ_i between 0 and $\pi/2$, recollision can take place.

3. *Recombination*: Recombination of the electron with its parent ion occurs under the emission of a high-energy photon γ. Applying Eq. 2.1 and 2.4 yields the kinetic energy of the photon

$$E_\gamma = 2 \cdot U_{\text{pond}}(\sin\varphi - \sin\varphi_i)^2. \tag{2.5}$$

The maximum photon energy, called cutoff energy, is reached for $\varphi_i = 0.31$ and can be graphically deduced [29] or numerically calculated [31] to

$$E_{\text{cutoff}} = 3.17U_{\text{pond}} + U_{\text{ion}}. \tag{2.6}$$

The process of HHG can happen twice per laser cycle, generating a train of even shorter pulses with a much higher energy than the energy from the driving laser field. In this way, odd harmonics are produced when focusing on an isotropic medium.

2.1.2 Phase Matching of HHG

In HHG, the nonlinear medium is ionized as the HH are emitted. In this process, the free electrons cause defocusing and phase mismatch, limiting the upconversion efficiency. Here, two concepts are essential. For one, dispersion. As waves at different frequencies can propagate at different velocities, they can get out of phase. The other concept is focusing. Focusing initiates a geometrical phase slip, which varies for the harmonic field and its driving polarization. To reach a highly efficient frequency conversion, the phase front of the generated field needs to match the phase front of the driving laser field. An illustration of the phase matching process is shown in Fig. 2.2. We can define the phase mismatch between the wave vector of the driving laser field $\mathbf{k}_1$ and the wave vector of the q^{th} harmonic $\mathbf{k}_\mathrm{q}$ as

$$\Delta\mathbf{k}(q) = q\mathbf{k}_1 - \mathbf{k}_\mathrm{q}, \tag{2.7}$$

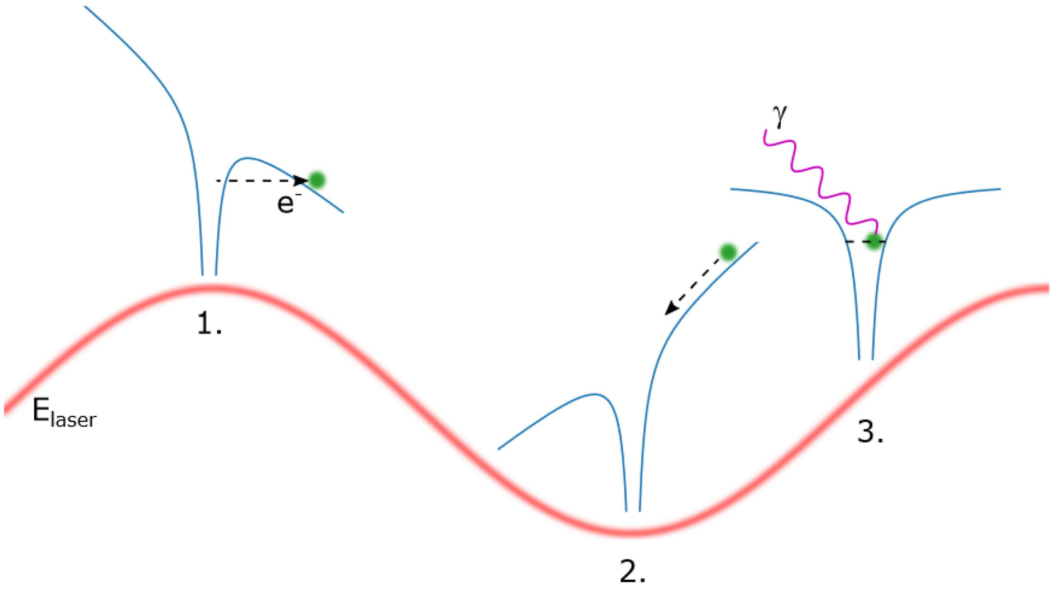

Figure 2.1: HHG: 1. The driving laser field (red) modifies the Coulomb potential (blue) of the atom such that an electron (green) can tunnel out and is accelerated. 2. The oscillating laser field accelerates the electron back to the atom. 3. The electron recombines with its parent ion under the emission of a high-energy photon. Taken from [8].

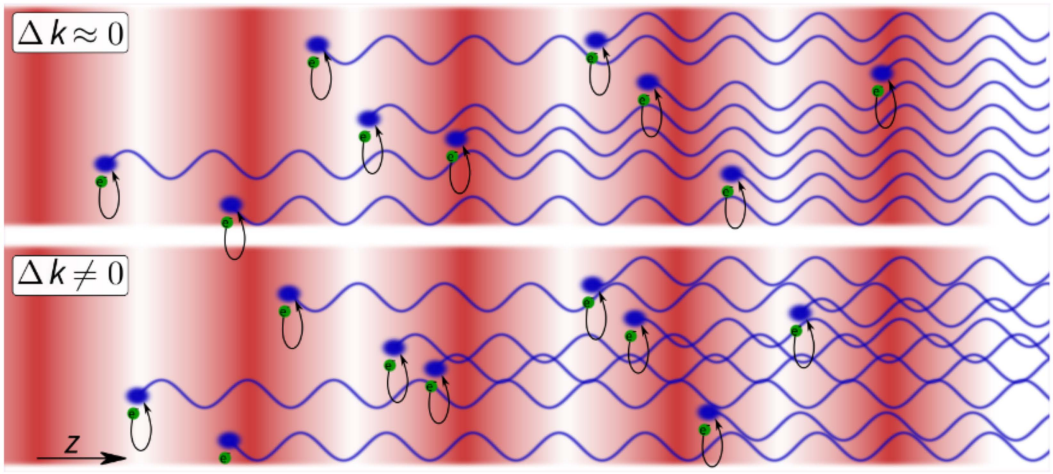

Figure 2.2: Schematic of the HHG phase-matching effect. Waves interfere constructively in the case of phase-matching, where $\Delta k \approx 0$. The HHG yield is increasing, whereas for non-phase-matched conditions, $\Delta k \neq 0$, the yield is low. Taken from [24].

knowing that the phase velocity of the qth harmonic is $v_q = q\omega_1/k_q$ and the phase velocity of the driving laser field is $v_1 = \omega_1/k_1$. $\Delta\mathbf{k}(q)$ usually changes slowly with frequency for HHG in gases. Therefore, group velocity mismatch effects can often be neglected.

Using a Gaussian laser beam, four contributions to the phase mismatch take place, which is given by the relation [32]

$$\Delta\mathbf{k} = \Delta\mathbf{k}_\mathrm{g} + \Delta\mathbf{k}_\mathrm{d} + \Delta\mathbf{k}_\mathrm{n} + \Delta\mathbf{k}_\mathrm{p}. \tag{2.8}$$

Thereby, $\Delta\mathbf{k}_\mathrm{g}$ describes the wave vector mismatch due to the Gouy phase. $\Delta\mathbf{k}_\mathrm{d}$ is the wave vector mismatch induced by the dipole phase arising from the electron trajectory. $\Delta\mathbf{k}_\mathrm{n}$ describes the neutral gas medium dispersion and $\Delta\mathbf{k}_\mathrm{p}$ the dispersion of the generated plasma. To generate a complete phase-matched harmonic signal, all four constituents need to be compensated by each other for all positions within the nonlinear medium, for all times t. Only the longitudinal component z along the optical axis will be considered for simplicity. In the following, all four factors contributing to phase mismatching are elucidated.

i) Δk_g - *Gouy phase*:
Propagating along the z direction, the Gaussian beam inherits a phase shift that differs from the phase shift for a plane wave with the same optical frequency [33]. This phase shift is called Gouy phase and is given by

$$\phi_\mathrm{Gouy}(r,z) = -\tan\left(\frac{z}{z_R}\right) + \frac{k_1 r^2}{2R(z)}, \tag{2.9}$$

where z_R is the Rayleigh length and $R(z) = z + z_R^2/z$ the beam radius of curvature. The resulting phase mismatch for the qth harmonic at the optical axis is

$$\Delta k_\mathrm{g} = q\left.\frac{\partial\phi_\mathrm{Gouy}(z)}{\partial z}\right|_{z\to 0} = -\frac{q}{z_R}. \tag{2.10}$$

For $z = 0$ the Gouy phase contribution reaches a maximum. As a consequence, adjusting the gas nozzle position with the laser focus allows fine-tuning the size of the Gouy phase shift as well as fine-tuning Δk_g, since near the laser focus, the Gouy phase contribution becomes rather small.

ii) Δk_d - *Dipole phase*:
The dipole phase induces the second contribution to the phase mismatch, resulting from the electron trajectory. Taking the quasi-classical limit into account, each electron trajectory gains an intensity-dependent dipole phase in the continuum, which is given by [34]

$$\phi_j(q,I) = q\omega_c t' - \frac{1}{\hbar}S(\mathbf{p},t,t'), \tag{2.11}$$

where q is the harmonic order, ω_c the laser angular frequency, t' denoting the duration of the electrons' trajectory and S the quasi-classical action. Approximating

Eq. 2.11 linearly with the space- and time-dependent intensity $I(r, z, t)$ yields

$$\phi_j(q, I) \approx \alpha_{0,j}(q) - \alpha_j(q) I(r, z, t). \tag{2.12}$$

From there, we can derive the wave vector mismatch:

$$\Delta k_d = -\alpha_j(q) \frac{\partial I(r, z)}{\partial z}. \tag{2.13}$$

Here, $\alpha_j(q)$ is positive. For short trajectories, the proportionality constant is small and can be neglected within the laser focus [35].

iii) Δk_n - *Neutral dispersion*:
The third component is the wave vector mismatch as a consequence of neutral gas dispersion, which is described by [36]

$$\Delta k_n = q \frac{\omega_c}{c} P(1 - \eta)(n_0 - n_q + n_2 I), \tag{2.14}$$

where P is the standard pressure, η denotes the ionization fraction, and n_0, n_q the refractive indices of the gas medium for the fundamental laser and the q^{th} harmonic, respectively. n_2 is the intensity-dependent index of refraction.

iv) Δk_p - *Plasma dispersion*:
The fourth contribution is the wave vector mismatch due to plasma dispersion. Since the recombination of the freed electron with the parent ion has a small probability, there are many free electrons. Thus, plasma is formed. Neglecting the dispersion from the ions due to their large mass and higher resonance frequency, the wave vector mismatch can be expressed as

$$\Delta k_p = -q \frac{\omega_c}{c} (n_{0,\mathrm{el}} - n_{q,\mathrm{el}}) \approx -q \frac{\omega_c}{2\pi c} p \eta N_a r_e. \tag{2.15}$$

N_a is the atomic number density, c the speed of light and r_e is the classical electron radius. $n_{0,\mathrm{el}}$ and $n_{q,\mathrm{el}}$ are the plasma refractive indices.

To understand how phase-matching affects the HHG yield, the coherent sum over all atoms in the nonlinear medium for each harmonic order q within the length of the nonlinear medium L_med has to be considered. The HHG yield S_q can then be expressed as [37]

$$\begin{aligned} S_q \propto \rho^2 A_q^2 \frac{4 L_\mathrm{abs}^2}{1 + 4\pi^2 (L_\mathrm{abs}/L_\mathrm{coh})^2} \\ \left[1 + \exp\left(-\frac{L_\mathrm{med}}{L_\mathrm{abs}} \right) - 2 \cos\left(\frac{\pi L_\mathrm{med}}{L_\mathrm{coh}} \right) \exp\left(-\frac{L_\mathrm{med}}{2 L_\mathrm{abs}} \right) \right], \end{aligned} \tag{2.16}$$

where A_q describes the amplitude of the atomic response at the qth harmonic. $L_\mathrm{abs} = (\sigma\rho)^{-1}$ is the absorption length, with σ being the ionization cross-section and gas density

ρ. $L_{\text{coh}} = \pi/\Delta k$ denotes the coherence length of the emitted radiation. If both, A_q and L_{abs}, are assumed to be constant over the generation volume. Equation 2.16 can be rewritten in the absence of absorption $L_{\text{abs}} = \infty$ as

$$S_q \propto L_{\text{med}}^2 \cdot \text{sinc}^2\left(\frac{\Delta k L_{\text{med}}}{\pi}\right). \tag{2.17}$$

To gain at least half of the maximum yield of HHG, the coherence length should be $L_{\text{coh}} > 5L_{\text{abs}}$ and the length of the nonlinear medium $L_{\text{med}} > 3L_{\text{abs}}$ [37].

2.1.3 Steady-State Plasma

XUV sources usually operate at low repetition rates $f_{\text{rep}} < 100\,\text{kHz}$ [37]. However, our frequency comb works at a significantly higher repetition rate of $f_{\text{rep}} = 100\,\text{MHz}$. Balancing neutral and plasma dispersion becomes demanding at repetition rates above $f_{\text{rep}} > 10\,\text{MHz}$ [38]. The reason for this is steady-state plasma, which is generated by one pulse. As the repetition rate is very high, the plasma can not be cleared before the next pulse arrives and, thus, generates even more plasma [39]. Hence, a high-density plasma is produced. This plasma is highly dispersive, which makes phase-matching impossible. Thus, it requires shortening the time the ions stay in the interaction region to minimize the steady-state ionization fraction η_{steady}. Reducing steady-state plasma is beneficial since it contributes to optical bistability and coupling to higher-order transverse modes due to plasma lensing. This limits the intracavity focal intensity [39]. Another problem is the phenomenon of intensity clamping, which arises from nonlinear effects, coming from the dynamics of ionization on a single-pulse timescale [40].

One solution is to increase the velocity of the target gas. For this reason, the formation dynamics of steady-state plasma have to be considered. The steady-state plasma is mainly characterized by the laser pulse repetition period $\tau_{\text{rep}} = 1/f_{\text{rep}}$. We define two dimensionless parameters [38]: $\xi_{\text{ion}} = \tau_{\text{ion}}/\tau_{\text{rep}}$ and $\xi_{\text{beam}} = \tau_{\text{beam}}/\tau_{\text{rep}}$. Where ξ_{ion} describes the number of laser pulses that enter the gas jet during the time it takes an ion to clear the ion-generation volume and ξ_{beam} denotes the number of laser pulses during the transit time of an atom through the laser beam volume. τ_{ion} marks the transit time of an ion through the full-width at half-maximum (FWHM) of the intensity-dependent ion-generation volume. $\tau_{\text{beam}} = \sigma_{\text{FWHM}}/v_{\text{gas}}$, where σ_{FWHM} is the FWHM of the intensity profile. The translational gas velocity perpendicular to the laser propagation is specified by

$$v_{\text{gas}} = \sqrt{\frac{5RT}{M_{\text{avg}}}}, \tag{2.18}$$

where R denotes the universal gas constant, T is the gas backing temperature and M_{avg} the weighted-average molar mass of the atomic gas mixture [39]. The gas velocity can be increased by increasing the gas backing temperature, which makes an intra-cavity nozzle at high temperatures necessary. Another possibility is to use gas mixtures. Seeding a

heavy generator gas in a light carrier gas decreases M_{avg} and therefore increases the gas velocity [39]. Usually, helium is chosen as the light carrier gas because of its light mass and high ionization potential. Using a He:Xe 9:1 mixture increases the velocity significantly [8, 23].

2.1.4 Pressure-induced Phase Matching

It is possible to compensate the neutral gas dispersion with the plasma dispersion as a function of the ionization fraction η since they have opposite signs. The critical ionization fraction describes the ionization fraction limit when both dispersions are compensated [41]

$$\eta_{\text{crit}} = \left(\frac{\lambda_0^2 N_a r_e}{2\pi(n_0 - n_q)} + 1 \right)^{-1}. \tag{2.19}$$

Ideal phase matching conditions can only be realized for ionization fractions below the critical value $\eta < \eta_{\text{crit}}$, because of the negative phase mismatch Δk_{g}, neglecting the wave vector mismatch induced by the dipole phase. The Gouy phase can be compensated through the gas density, which allows alteration of the dispersion contribution. Equation (2.8) can be described by

$$P_{\text{match}} \left[\frac{\partial \Delta k_n}{\partial P} + \frac{\partial \Delta k_p}{\Delta P} \right] + \Delta k_g = 0. \tag{2.20}$$

Here, the gas density is assumed to be linearly dependent on the pressure. The phase matching pressure within the laser focus is given by [42]

$$P_{\text{match}} = P_0 \frac{\lambda_0^2}{2\pi^2 w_0^2 \Delta(n_0 - n_q)(1 - \eta/\eta_{\text{crit}})}, \tag{2.21}$$

where P_0 denotes the standard pressure $P_0 = 101.3\,\text{kPa}$, λ_0 the central wavelength of the driving laser field, w_0 the gaussian beam size and the plasma refractive index values n_0 and $n_q = \sqrt{1 - N_{\text{e}}/N_{\text{c}}}$. N_{e} describes the free electron density and can be calculated by ADK theory [43]. The critical density $N_c = \varepsilon_0 \omega^2 / e^2$ is the density at which the plasma frequency $\omega_{\text{p}} = \sqrt{N_e e^2/(m\varepsilon_0)}$ equals the laser frequency. At this density, the plasma becomes opaque to electromagnetic waves of frequency ω.

Since the phase matching pressure scales inversely with the square of the beam radius w_0 and inversely with the ionization fraction (Eq. 2.21), tight focusing requires large pressures in the interaction region. As a consequence, gas consumption becomes very high. Therefore, a gas recycling system is necessary in order to run measurements over several weeks which is needed in our case.

2.2 Model Conceptions of Gases

This section covers the behavior of gases at different pressures. First, the ideal gas is discussed in case of low pressure. Next, high-pressure gases are described, where the ideal gas model is not applicable. Last, leakage rates of gases are treated, where it has to be differentiated between the ideal gas model and the real gas model.

2.2.1 Ideal Gas

In atmospheric conditions (<= 1013.25 mbar), the model conception of a "liquid" gas flow is applicable, also known as *continuum theory*. The gas can be described by differential changes in macroscopic quantities, such as velocity, density, pressure and temperature. However, the description of the model fails if the gas is highly diluted, which is the case in a vacuum environment. This is because the local mean values can depend on the instantaneous state of individual molecules. To be able to describe this, a microscopic observation is necessary.

The transition to a statistical approach makes it possible, despite the vast number of molecules in a gas, to infer and calculate the macroscopic properties of the gas from the microscopic states. This theory is known as *kinetic theory* [44]. It makes the following basic assumptions:

- Atoms and molecules are point-like.
- Forces are exclusively transmitted during impacts.
- Impacts are elastic.
- Molecular disorder takes priority.

From these assumptions, it becomes clear that gases at low pressure can be described by the ideal gas model, which neglects interactions between gas molecules. The ideal gas law was first stated by É. Clapeyron [45] and is given by

$$PV = Nk_{\mathrm{B}}T, \tag{2.22}$$

where $k_{\mathrm{B}} = 1.380\,649 \times 10^{-23}\,\mathrm{J\,K^{-1}}$ denotes the Boltzmann constant, P the pressure, V the volume, T the temperature and N the number of particles. The relation between the mass m_p of a gas particle and the molar mass M is

$$M = N_{\mathrm{A}} \cdot m_p, \tag{2.23}$$

where $N_{\mathrm{A}} = 6.022\,140\,76 \times 10^{23}\,\mathrm{mol^{-1}}$ denotes the Avogadro constant. Further, the gas constant can be described by

$$R = N_A \cdot k_{\mathrm{B}}. \tag{2.24}$$

From Eq. 2.22 and 2.24 follows the ideal gas law for one mol of a gas

$$PV = RT. \tag{2.25}$$

In kinetic theory, the mean free path is used to characterize different types of flow. It is defined as

$$\lambda = \frac{1}{\sqrt{2}n\sigma}, \tag{2.26}$$

where $n = N/V$ is the number of molecules per volume and σ the collision cross-section. For low-pressure gases, three types of flow can exist, *viscous flow* (6.0×10^{-1} mbar cm), *molecular flow* (1.3×10^{-2} mbar cm) and *Knudsen flow* (1.3×10^{-2} mbar cm)[44]. Molecular flow is predominant in the high - and ultra-high vacuum range. In these regimes, the molecules can move freely without obstructing each other. This means that molecular flow is only present when a particle's mean free path length is much greater than the diameter of the tube. The transition from viscous flow to molecular flow is the so-called Knudsen flow. It prevails in the fine vacuum region, where the mean free path length is approximately equal to the diameter of the tube.

2.2.2 Real Gas

The ideal gas model is no longer applicable for high-pressure gases ($\gg 1$ bar). The reason for this is the higher density of gases at high pressures. As a result, the interactions of atoms must be addressed. The Van der Waals equation can model these real gases. It extends the ideal gas law to take interactions between atoms of gas into account as well as the finite size of the atoms. Let b be the molar volume of gas atoms in L mol^{-1}. If we want to account for the real gas volume, we need to replace the volume in the ideal gas law 2.22 by $V_{\text{corr}} = V - nb$. This leads to

$$P(V - nb) = nk_{\text{B}}T. \tag{2.27}$$

The second modification considers the interactions between molecules and corrects the pressure in the ideal gas law. From Eq. 2.25 follows the pressure for one mole of a gas

$$P = \frac{RT}{\frac{V}{n} - b}. \tag{2.28}$$

In the following, we assume that we have a container filled with gas. To consider the attractive force between the molecules, we make the assumption that the net force on a surface molecule, pulling it into a container, is proportional to the number density

$$C = \frac{nN_{\text{A}}}{V}. \tag{2.29}$$

The force on the container walls is decreasing by a factor proportional to the square of the density. Therefore, the pressure decreases by the factor [46]

$$a'C^2 = a'\left(\frac{nN_A}{V}\right)^2 = \frac{an^2}{V^2}, \tag{2.30}$$

where a is the Van der Waals constant for a specific gas. The values for selected gases for both constants, a and b, are shown in Table 2.1. Rewriting Eq. 2.28 yields

$$P = \frac{RT}{\frac{V}{n} - b} - \frac{an^2}{V^2}. \tag{2.31}$$

Rewriting this formula gives the Van der Waals equation

$$\left(P + \frac{an^2}{V}\right)(V - nb) = nRT. \tag{2.32}$$

Gas	a ($\mathrm{L^2\,mol^{-2}}$)	b ($\mathrm{L\,mol^{-1}}$)
He	0.0346	0.0238
Ar	1.355	0.03201
Kr	2.325	0.0396
Xe	4.192	0.05156

Table 2.1: Van der Waals constants [47] for selected gases.

2.2.3 Modeling Gas Leakage Rates

A system filled with gas is never completely leak-tight under real conditions. For this reason, it is important to keep the leakage rate q low enough to not affect the final pressure. Leakage rates are usually measured in units of $\mathrm{mbar\,L\,s^{-1}}$. Another variant is to describe the leakage rate in standard liters (SL) per hour. A standard liter describes one liter of gas at atmospheric pressure (1013.25 mbar).

To compare leakage rates between different gas types, it must be taken into account that different equations apply to viscous and molecular flow. For a viscous gas flow the leakage rate can be compared by [44]

$$q_\mathrm{A} \cdot \eta_\mathrm{A} = q_\mathrm{B} \cdot \eta_\mathrm{B}, \tag{2.33}$$

where η denotes the dynamic viscosity constant and A and B are two different gases. As a guideline, for leakage rates in the range of $q > 10^{-5}\,\mathrm{mbar\,L\,s^{-1}}$ viscous flow is applicable and for $q < 10^{-7}\,\mathrm{mbar\,L\,s^{-1}}$ molecular flow. For leakage rates, where molecular flow is applicable, the conversion between leakage rates between gas types is given by [44]

$$q_\mathrm{A} \cdot \sqrt{M_\mathrm{A}} = q_\mathrm{B} \cdot \sqrt{M_\mathrm{B}}, \tag{2.34}$$

where M is the molar mass. With these equations, we can compare leakage rates between different gas species. In addition, the leakage rate is almost always dependent on the pressure difference.

3 Experimental Setup

This chapter describes the experimental setup of the gas recycling system. First, a brief overview of the femtosecond enhancement cavity (fsEC) is given. Second, the differential pumping system, which is necessary to keep low pressures while gas is injected, is presented. Third, the gas recycling system with its three compartments is described.

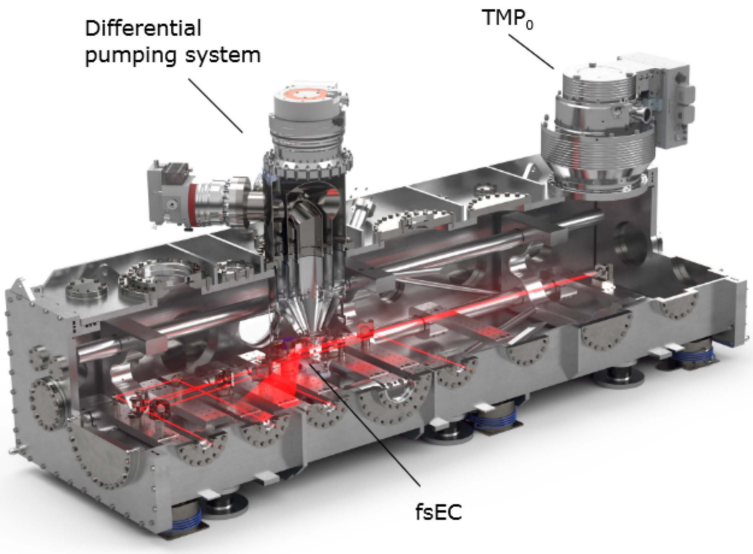

Figure 3.1: Overview of the vacuum chamber. The differential pumping system surrounds the laser focus of the fsEC [48]. The laser beam is indicated in red. The vacuum chamber is pumped by an additional turbomolecular pump (TMP$_0$).

3.1 Femtosecond Enhancement Cavity

To reach intensities of about $10^{14}\,\mathrm{W\,cm^{-2}}$, sufficient to generate HH, the pulses that are emitted from the amplified frequency comb laser have to be further enhanced. For this reason, a fsEC was developed [8, 10]. First, the fsEC setup is treated and finally, the limiting effect of mirror degradation is discussed.

3.1.1 fsEC Setup

In Fig. 3.1, an overview of the setup is shown. It consists mainly of five optical elements. Since additional mirrors lead to increased NIR dispersion and scattering losses, a reduced number of optical elements is beneficial. An astigmatism-compensated bow-tie cavity was chosen because of its non-linear cavity design, which allows tight focusing (for more information, see [10]). The pulses are coupled in by an input coupler (IC), then reflected and focused at curved mirror 1 (CM1). Subsequently, reflected at a grating mirror (GM), reflected and focused at CM2 and passing a piezo-driven flat cavity mirror (FPM) and finally, back to the IC. The GM couples out the HH. For a repetition rate of 100 MHz, the total path length of the cavity measures exactly 2.997 924 58 m, allowing consecutive pulses to interfere constructively. To enhance the pulse train, all spectral components have to be in resonance simultaneously. The envelopes of the overlapping pulses and the underlying carrier need to interfere constructively. An overview of the optical elements inside the main chamber is shown in Fig. 3.2. To stabilize the length of the cavity to the comb repetition rate, the Pound-Drever-Hall method is applied. For this purpose, the cavity reflected beam is used as the input for a feedback loop that corrects the cavity length by adjusting the piezo mirror position.

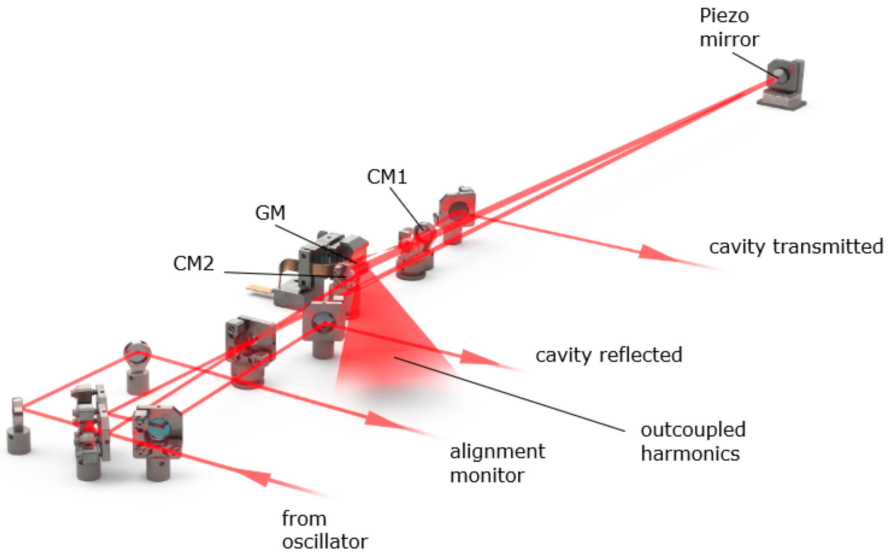

Figure 3.2: fsEC setup inside the main chamber. The cavity reflected beam is used to correct the cavity length by adjusting the piezo mirror position, applying the Pound-Drever-Hall method. Adapted from [8].

3.1.2 Gas Injection System

The target gas for HHG is injected through a quartz nozzle with an inner diameter in the range of 30 to 100 µm into the laser focus and caught by the differential pumping system, as shown in Fig. 3.3. To inject the gas into the laser focus, a gas panel (GP) was designed. It consists mainly of a pressure regulator to set the backing pressure for the gas nozzle, a digital pressure gauge to monitor the pressure and a particle filter to clean the target gas from contamination. An overview is shown in Fig. 3.6 a). A scroll pump allows to remove the gas, confined at the GP, necessary when switching between gas species.

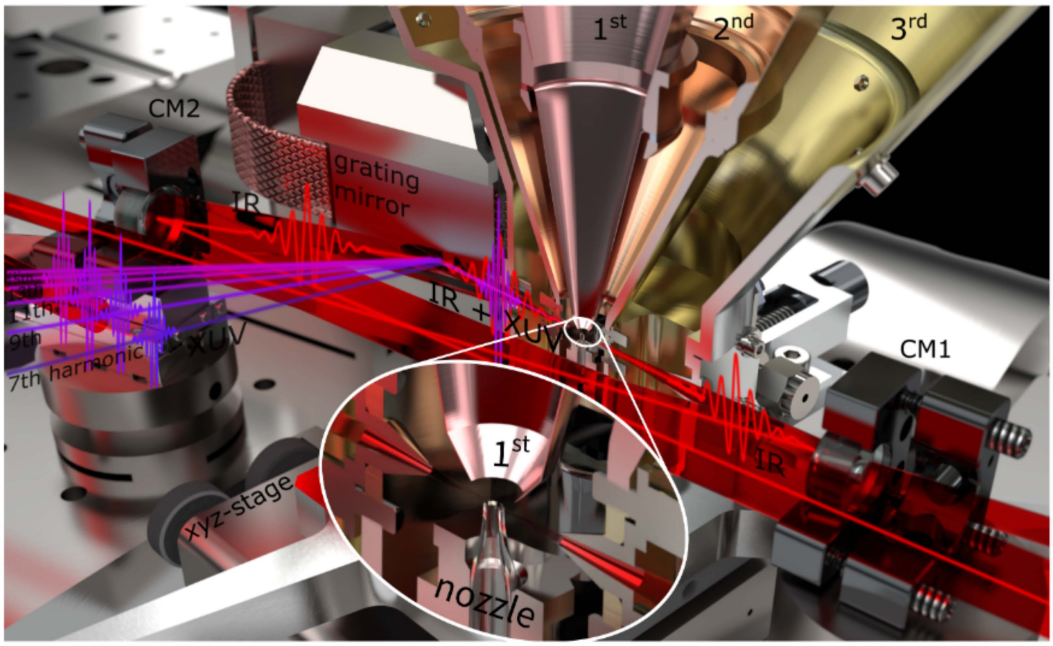

Figure 3.3: Overview of the laser focus area. The gas is injected by a quartz nozzle into the laser focus and caught by the differential pumping system. HH are coupled out by the GM. Taken from [24], adapted from [8].

The XUV generation inside the fsEC is limited by the degradation of the cavity mirrors and outcoupling optics. Residual molecules inside the vacuum chamber are present, containing hydrocarbon chains. These chains can get cracked by XUV radiation and secondary electron excitation, afterwards sticking to the mirror surfaces. For optics exposed to XUV radiation, such as the grating mirror in our experiment, this leads to a thin layer, degrading the optical properties [49]. The grating structure of the output coupler is affected strongly by these thin films since the shallow grooves fill with contamination, which deteriorates the GM structure. This results in a substantial decrease in outcoupled harmonic yield compared to the maximum harmonic yield [38].

One solution to this problem is to prevent hydrocarbon molecules from coming too close to optics. Ultra-high vacuum (UHV) conditions are essential for the reduction of hydrocarbons. To make sure that after a long XUV operation time, the optics will not degrade eventually even though the system is operated at good vacuum conditions, an ozone injection system, shown in Fig. 3.4 has been installed to clean the optics inside the fsEC [8]. Ozone can remove surface contaminants by oxidization [38]. Thereby, high-purity oxygen from a bottle is fed into an ozone generator[1] with a pressure of about 200 mbar. The ozone generator produces about 2% ozone at a flow rate of $0.5\,\mathrm{L\,min^{-1}}$. After passing the ozone generator, the ozone is filtered by an ozone-destroying catalyst[2]. A needle valve regulates the flow. Four nozzles with a 400 µm diameter are located inside the main chamber, pointing at the GM, CM2, IC and FPM. A scroll pump is connected to the system to clear the ozone injection system from residual gases before operation. The ozone present in the chamber can be monitored with a mass spectrometer. Considering that the mass spectrometer is about 0.5 m from the closest nozzle, the local ozone concentration at the mirror surface might be higher than measured.

3.2 Differential Pumping System

To generate HH, a vacuum environment is required since XUV radiation is extensively absorbed by air. Additionally, a strong decrease of hydrocarbon abundance, due to UHV conditions, prevents the optics from mirror degradation [38]. The MC will have a direct connection to CryPTex-SC [12], where a pressure of 10^{-14} mbar is required. Since the target gas is injected at a pressure of about 10 bar, efficient differential pumping is required to bridge the pressure gap. Another difficulty arises from the HHG efficiency, which is highly dependent on the density of the target gas. Mixing the HHG target gas with a much lighter gas, such as helium, increases the velocity of the gas, as described in Subsection 2.1.3. Consequently, multiple interactions of a single atom of the target gas with the laser pulses can be avoided. However, the pressure needs to match the factor equal to the mixing ratio of these two gases. By using a 9:1 He:Xe mixing ratio, a backing pressure of about 90 bar is necessary to achieve a xenon partial pressure of 10 bar. This indicates that a large amount of gas must be injected into the vacuum chamber, which deteriorates the vacuum and requires high pumping power.

For this reason, a differential pumping system was built, shown in Fig. 3.5, consisting of three stages surrounding the cavity focus [8, 48, 50]. Thin, conical-shaped walls space the three stages to maximize the pumping speed. Each stage is connected to a separate turbomolecular pump (TMP). Where the pumping speeds for the first, second and third stage are $\mathrm{TMP_1}$: $300\,\mathrm{L\,s^{-1}}$, $\mathrm{TMP_2}$: $440\,\mathrm{L\,s^{-1}}$ and $\mathrm{TMP_3}$: $1300\,\mathrm{L\,s^{-1}}$, respectively. All of the pumps possess a magnetic bearing for reduced vibrations.

[1] Ozotech Poseidon 220
[2] CARULITE 200

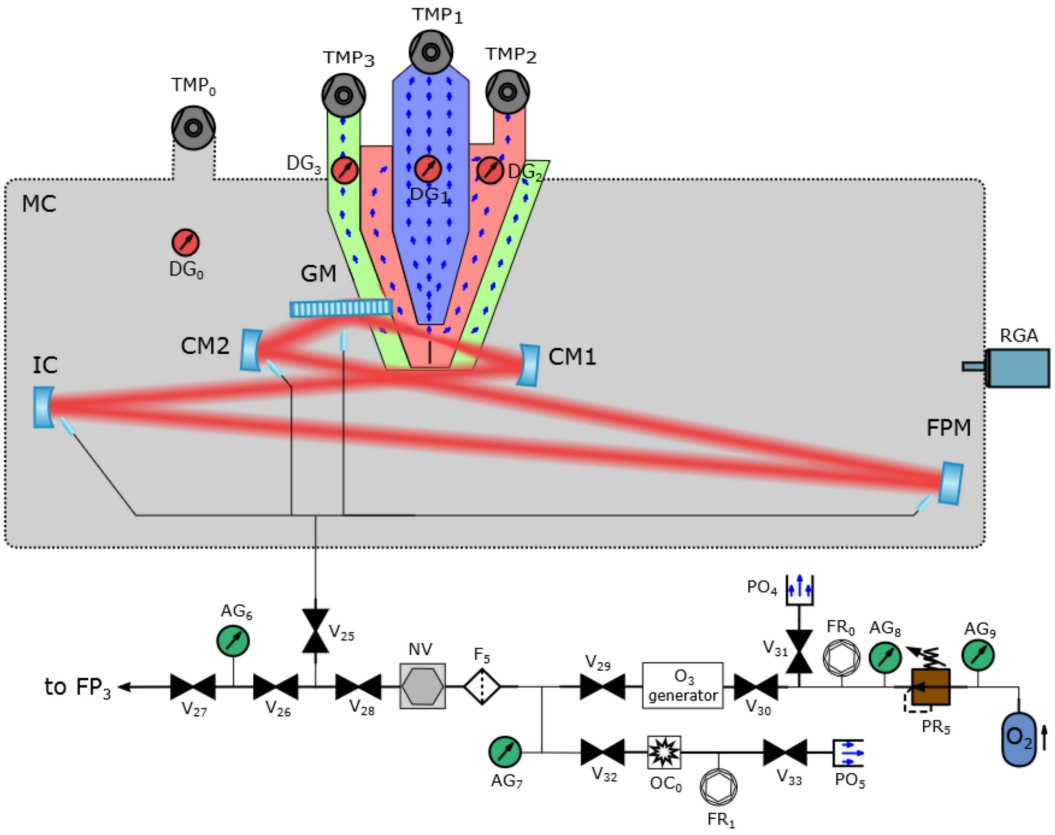

Figure 3.4: Overview of the ozone injection setup. The fsEC setup is shown inside the MC. The differential pumping system is surrounding the laser focus. The light comes through the IC and goes to the first CM. Afterwards, the light is reflected at the GM, where the HH are coupled out. After passing the GM, the pulses pass CM2, next to the piezo-driven flat cavity mirror and finally to the IC again, where the pulses interfere with the next pulse emitted from the laser source. The ozone system is depicted on the outside of the MC. A regulated flow from an oxygen bottle is fed into an ozone generator. The amount of the ozone mixture is regulated (flow regulator: FR) by a needle valve (NV). Residual ozone is removed by an ozone catalyst (OC) before the outlet.

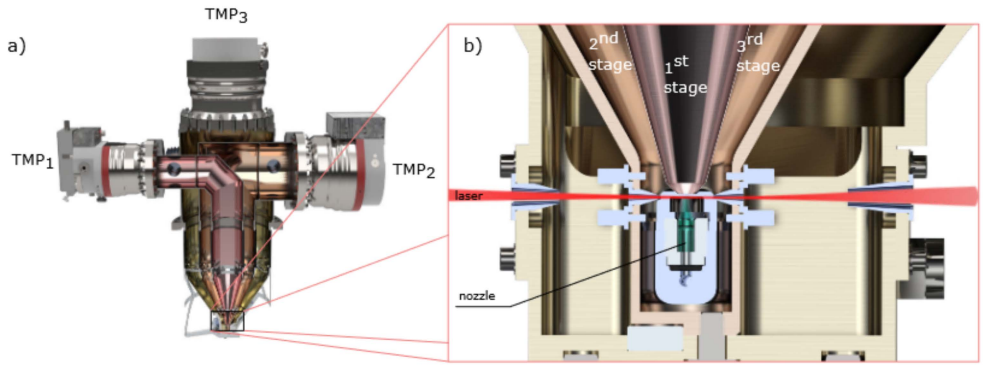

Figure 3.5: a) overview of the differential pumping system. The three pump stages, spaced by conical-shaped walls, increase the pumping efficiency. b) close-up of the lower part of the differential pumping system. The pumping system surrounds the laser focus. The target gas for HHG is injected through the nozzle below the laser focus. Adapted from [8].

As a compromise between undisturbed cavity mode and the highest gas pressure, we placed a gas nozzle at about 100 µm at a vertical distance. To adjust the gas nozzle position, the lower part of the pumping system is mounted on a translation stage. This stage can be moved in steps of 30 nm by five pico-motors in the xyz directions, as well as in the θx and θy direction. A skimmer can capture a large amount of the emerging vertical gas jet in the first stage at a vertical distance of 0.5 mm from the nozzle. The second stage was built symmetrically, enclosing the nozzle and supporting the skimmer. Due to space constraints, the third stage was built asymmetrically. The laser enters and exits the interaction region through holes in the second and third stage, as shown in Fig. 3.5 b).

3.3 Gas Recycling Setup

Generating HH inside the enhancement cavity requires a continuous supply of gas. Frequently, xenon is used as a target gas because of its low ionization potential. The need for a high flow rate in high-repetition-rate systems makes this very costly in the order of several thousand euro per day. As long operation times are needed to collect enough statistics for spectroscopy measurements, a gas recycling system was built [23]. The whole setup is depicted in Fig. 3.6. It consists of three main compartments: a low pressure system (LPS), a compressor station (CS) and a high pressure system (HPS). It allows compressing gas up to 200 bar. A list of the components used in the setup is shown in Table 3.1.

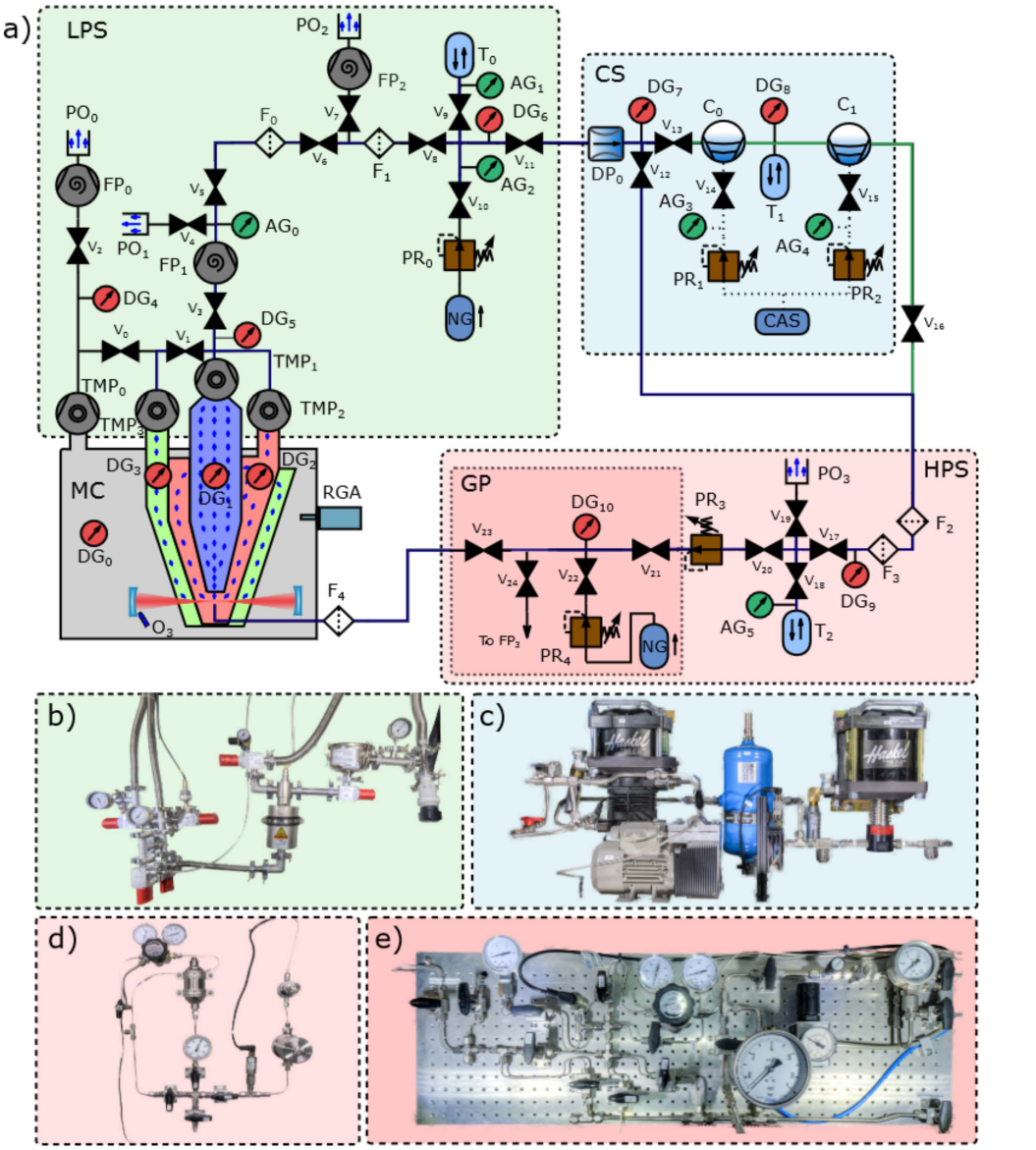

Figure 3.6: In a), an overview of the gas flow in the system is shown. The gas recycling setup is divided into mainly three compartments: LPS: low-pressure system ($0 - 1\,\mathrm{bar\,abs}$), CS: compressor station, HPS: high-pressure system (max. $200\,\mathrm{bar}$), GP: gas panel (max. $200\,\mathrm{bar}$). The main compartments are labeled as follows: turbo-molecular pump (TMP), fore-vacuum pump (FP), diaphragm pump (DP), storage/buffer tank (T), filter (F), compressor (C), residual gas analyzer (RGA), pressure outlet (PO), pressure regulator (PR), analog/digital pressure gauge (AG/DG), valve (V), main vacuum chamber (MC). The compressors are driven by the compressed air supply (CAS) of the institute. In b), c), d) and e) photographs of the LPS, CS, HPS and GP are shown, respectively.

Vacuum pumps and compressors			Filters, gauges, detectors		
Abbr.	Company	Type	Abbr.	Company	Type
TP_0	Leybold	Turbo pump MAG W 2200	F_0	Agilent	Particle filter SCRINTRPNW25
TP_1	Edwards	Turbo pump STPH 301C	F_1	Vacom	Adsorption trap FT25KF-J
TP_2	Edwards	Turbo pump STP 451-3	F_2	Parker Balston	Particle filter Model 95S6
TP_3	Leybold	Turbo pump MAG W 1300	F_3	Parker Balston	Activated carbon filter Model EU37/12
FP_0	Edwards	Scroll pump XDS35i	F_4	Swagelock	Particle filter 0.5 µm
FP_1	Pfeiffer	Roots pump A100L	$DG_{0,1,2,3}$	Agilent	FRG-730 full range Pirani Bayard-Alpert
FP_2	Edwards	Scroll pump XDS7i	$DG_{4,5,6}$	Agilent	ConvecTorr thermocouple gauge
MP_0	Hyco	diaphragm pump MP65-GD-W14	$DG_{7,10}$	RS PRO	Model 175-4981 (-1 + 24 bar)
C_0	Haskel	Gas booster AAD-5-HD	DG_9	RS PRO	Model 175 - 4995 (0 - 250 bar)
C_1	Haskel	Gas booster AAD-30	DG_8	RS PRO	Model 175 - 4992 (0 - 25 bar)
			RGA	MKS	Residual gas analyzer Microvision 2

Table 3.1: Components used in the gas recycling setup.

3.3.1 Low Pressure System

In the LPS, the gas is mainly purified from possible contaminants, which are inside the MC. Therefore, the gas caught by the differential pumping system is led to one of the fore-vacuum pumps $FP_{0,1}$, depending on the valve settings V_{0-3}. To recycle all of the gas, which is inside the MC, TMP_0 can be added as an additional pump by opening $V_{0,2,3}$ and closing V_1. Recycling the gas with the differential pumping system only, the valves V_{1-3} are opened and V_0 is closed. To direct the gas further into the LPS, it requires opening valves $V_{1,3,5}$. It consists of two filters ($F_{0,1}$) and a 20 L tank (T_0). After passing the first fore-vacuum pump (FP_1), it is possible to either lead the gas out of the system through exhaust ports ($PO_{1,2}$) or to confine the gas in the LPS. The gas passes through a particle filter (F_0) and an adsorption trap (F_1), which filters water and oil (for more information, see Subsection 3.3.4). Thereafter, the cleaned gas can be stored in T_0. To put the system into operation or to compensate for losses, a gas bottle is connected to the LPS via V_{10}, which allows filling the system with gas. Opening V_{11} allows directing gas towards the CS. The total volume of the LPS is about 22.2 L. AG_{0-2} and DG_{4-6} monitor the LPS pressure. Since DG_6 is not working properly, especially for pressures in the range of 0 mbar, a camera records the pressure at AG_2. The images of AG_2 are converted to pressure values with a python script.

3.3.2 Compressor Station

A gas pressure between 5 and 50 bar is required for phase matching the HHG process, which makes gas compression necessary. Therefore, the CS[3] is used to compress the gas, consisting of a diaphragm pump (DP_0), a tank (T_1) and two compressors $C_{0,1}$. The DP has Viton seals, with a specified leaking rate of $1 \times 10^{-3}\,\mathrm{mbar\,L\,s^{-1}}$, allowing to boost the pressure by roughly 4 bar. The compressed air supply of the institute drives the compressors. The pressure of the compressors can be regulated by $PR_{1,2}$. After the gas leaves the DP, which is used as an input booster for the CS, it is directed into the two-stage piston compressor C_0, where the gas reaches a pressure of up to 10 bar. The gas is then stored in a 2 L tank T_1. DG_8 is employed to monitor the pressure at T_1 and DG_7 to record the pressure at DP_0. C_1 compresses the gas further to a pressure of up to 200 bar. To avoid contamination of the gas, the compressors are sealed with oil-free graphite seals. However, the microscopic gap due to the movement of the pistons inside the cylinder might not be entirely air sealed, which can lead to gas leaks. Additionally, the compressors must be operated at low frequencies (≤ 1 Hz) to avoid premature wear to friction. Because of the leak-affected compressors, a path was implemented to skip both compressors by opening V_{12} and closing V_{13}, "V_{skipC}". The gas can then be led directly towards the HPS, depicted by the blue line in Fig. 3.6 a). One limitation is DP_0 since it needs $150 - 200$ mbar to provide enough pressure for C_0.

[3] HD-tech, custom model

3.3.3 High Pressure System

When the gas enters the HPS, it is cleaned by the particle filter F_2, followed by the activated carbon filter F_3. Opening V_{18} allows storing gas in a 75 cm^3 tank T_2. T_2 serves as a buffer to prevent the piston impacts of the compressors from being transmitted to the gas nozzle. It is also possible to lead the gas out of the system through V_{19}. DG_9 and AG_5 are monitoring the pressure at the HPS.

The GP is used to lead the gas through a pressure regulator, which allows setting the backing pressure for the gas nozzle. It is also possible to inject the gas directly from a gas bottle towards the nozzle.

3.3.4 Components Used

Pressure Gauges

To characterize the efficiency of the recycling system, it is crucial to read out the pressure at various instances via pressure gauges. In view of the fact that the pressure changes by multiple orders of magnitude throughout one cycle, four different types of pressure gauges are used, which are listed in Table 3.1.

Here, DG_{0-6} produce a digital signal, whereas DG_{7-10} generate an output current between 4 and 20 mA, depending on the pressure. Since the latter gives out an analog signal, the analog-to-digital converter (ADC) units need to be converted into pressure units. For this reason, a converter box has been built. More details can be found in [25]. This box includes four input plugs, four independent voltage sources providing the gauges with the required voltage of 12 V and a 4-channel, 4 to 20 mA ADC converter shield connected to an Arduino-Nano board.

DG_{7-10} use a piezo-resistive ceramic sensor. The basic concept of a piezo-resistive sensor is to use the change in the electrical resistance of a material when stretched to measure the pressure. Ceramic is used because it is a material with high elasticity, corrosion resistance, wear resistance, impact, vibration resistance and good thermal stability characteristics. The ceramic pressure sensor mainly comprises a ceramic ring, a ceramic diaphragm and a ceramic cover plate. The ceramic diaphragm acts as a sensitive elastic body. A thick film process technology is used on the diaphragm to form a Wheatstone bridge as the sensor circuit. The Wheatstone bridge is a device for measuring electrical resistances. The bridge generates a linear output signal proportional to the pressure.

Filter

To reduce possible oil and water contamination in the system, five filters are used. In our experiment three filter types are used, which will be introduced in the following.

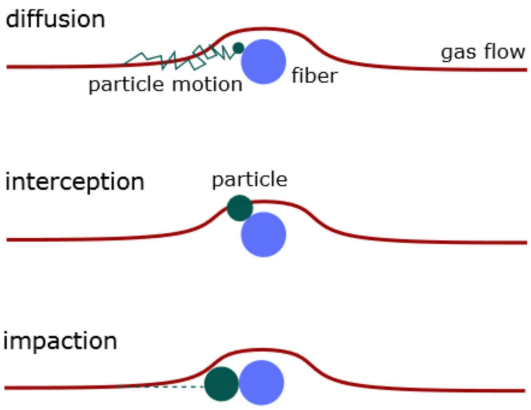

Figure 3.7: Working principle of a HEPA filter. The process of particle separation can be carried out in three different ways: diffusion, interception and impaction.

- *High-efficiency particulate absorbing (HEPA) filter*:
  HEPA filters remove particles with a diameter smaller than 1 µm. They are composed of a mat of arbitrarily arranged fibers consisting of polypropylene or fiberglass. F_0 is such a HEPA filter. The process of particle separation can be carried out in three different ways, which are also shown in Fig. 3.7:
  - Diffusion: Small particles with a size below 0.1 µm do not follow the gas flow line and collide with the molecules around. Thus, they collide with the filter fibers, where they keep sticking. The dynamics are comparable to Brownian motion.
  - Interception: Particles following the flow of gas cling to the fiber if they are close enough. Particles above 0.4 µm are caught by this process.
  - Impaction: Bigger particles (above 0.4 µm) do not follow the gas flow because of their inertness. Therefore, they collide with the fiber and adhere to it.
- *Adsorption trap filter*:
  An adsorption trap filter, such as F_1, is typically filled with zeolith. This material has pores with a diameter similar to the size of small molecules. Polar molecules get stuck in the zeolite zones because of cations inside the material and cannot leave the filter. Atoms, such as noble gases, are small enough to enter and exit the filter. In addition, the filter can be cleaned and regenerated by baking it out.
- *Activated carbon filter*:
  Activated carbon is processed in such a way that carbon develops low-volume pores. As a result, the surface area increases, which benefits the availability of adsorption or chemical reactions. Within this surface, contaminants can be trapped. F_3 is such an activated carbon filter.

Residual Gas Analyzer

A residual gas analyzer (RGA) monitors low levels of residual gas, which remain in the vacuum chamber after the pump-down. Thus, it can be employed to measure if the target gas is being recycled as well as if there are leaks in the system.

For our RGA, the principle of quadrupole mass spectrometry is used. Figure 3.8 shows an overview. This has the advantage of monitoring several gas-phase species in real-time. An RGA consists of a sensor, an interface box and a controller. In the sensor, a beam of ions is produced by electron impact ionization from a hot cathode. The extracted ion beam is directed into a quadrupole separation system with four rod-shaped electrodes. The cross sections of the four rods form the circles of curvature of a hyperbola so that the surrounding electric field is approximately hyperbolic. Two opposite rods each have the same potential, namely a direct voltage and a superimposed, high-frequency alternating voltage. This superposition of voltages generates the electric field ϕ [51]:

$$\phi = (U + V \cdot \cos \omega t) \cdot \frac{x^2 - y^2}{2r_0^2}, \tag{3.1}$$

where U is a DC voltage and $V \cdot \cos \omega t$ an AC voltage. The deflection from the trajectory of electrically charged particles is only possible according to their mass-to-charge ratio m/q because the attraction of the particles is proportional to their charge, but the oppositely acting inertia is proportional to their mass. The mass number of the ions, which are passing the separation system, have to fulfill the following condition [52]:

$$\frac{m}{q} \approx M = \frac{V}{14.438 \cdot f^2 \cdot r_0^2}, \tag{3.2}$$

where V denotes the high-frequency amplitude, r_0 the radius of the quadrupole rods, q the charge and f high-frequency. As a consequence of this linear dependence, a mass spectrum with linear mass scale by simultaneous and proportional change of U and V is obtained.

After leaving the separating system, the ions hit the ion catcher (a Faraday cup). Ions hitting the detector are neutralized by electrons from the ion catcher. As the actual measurement signal, the corresponding electrically amplified current is displayed as "ion current".

Compressor

To recompress the target gas, two compressors are implemented in our system. An overview of the working principle is shown in Fig. 3.9. Two valves inside the compressor cylinder prevent the gas from flowing backwards. If the pressure before the compressor p_{in} is larger than the pressure inside the cylinder p_{C1}, the inlet valve $\mathrm{V_{in}}$ opens because of this pressure gradient. On the contrary, the outlet valve $\mathrm{V_{out}}$ closes because $p_{\mathrm{C1}} < p_{\mathrm{out}}$,

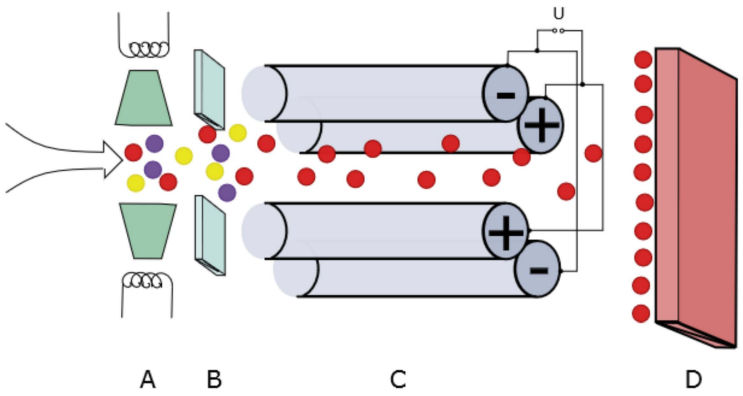

Figure 3.8: Working principle of a RGA. First, the electrons are emitted by a hot filament and collide afterwards with the incoming molecules and atoms forming ions, as shown in A. An electrostatic lens, shown in B, transports the charged particles to the quadrupole mass filter. There, the ions are separated according to their m/q ratio, as indicated in C. Lastly, the ions are detected by a Faraday cup, shown in D.

while the piston moves to the upper position. After the piston reaches its upper limit, the movement reverses and the confined gas inside the cylinder compresses. This increasing p_{C1} leads to closing $\mathrm{V_{in}}$ and opening $\mathrm{V_{out}}$. The confined gas is directed out of the compressor and the process can be repeated. The piston movement can be regulated by the CAS.

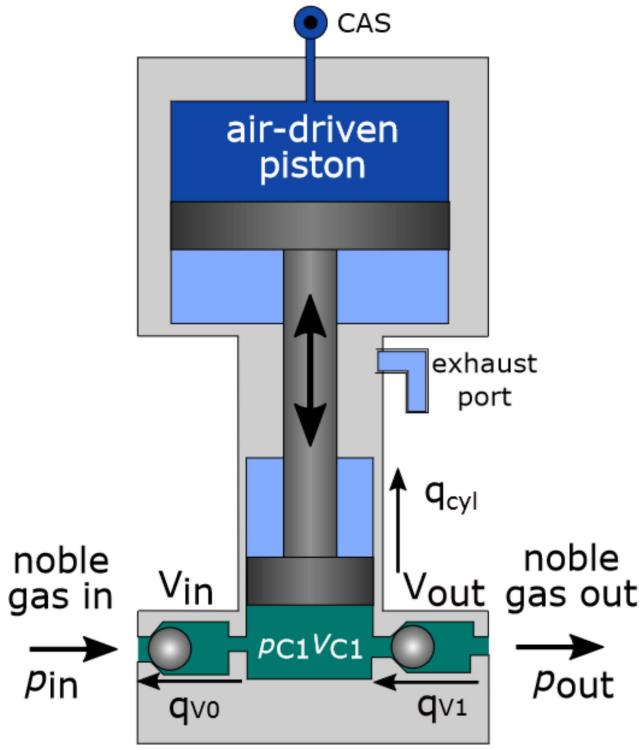

Figure 3.9: Schematic overview of C_1. The output pressure p_{out} of the compressor can be regulated by the CAS, shown in dark blue. The pressure inside the cylinder p_{C1} is depicted in the green shaded area. Two valves at the inlet V_{in} and outlet V_{out} prevent the gas from flowing backwards. If gas enters the compressor, V_{out} opens while V_{out} is closed and the piston moves upwards. The piston reverses the movement after reaching the upper position, therefore compressing the confined gas in the cylinder until the pressure inside the cylinder p_{C1} matches p_{out}. Because of the increasing pressure inside the cylinder, V_{out} opens and V_{in} closes. In this way, the gas is led out of the compressor. The leakage rates are indicated with "q". Adapted from [24].

4 Analysis

In this chapter, the leakage rates of the different parts of the system are quantified. Furthermore, the efficiency of the gas recycling system is evaluated by recycling argon and krypton.

4.1 Leakage Characterization

For characterizing the leakage rates of the system, it is crucial to know the inner volumes as accurately as possible. A summary of the volumes for the different parts in our system is given in Tab. 4.1. With these volumes, the leakage rates of the different parts of the system can be calculated by

$$q = V\frac{\Delta P}{\Delta t}, \tag{4.1}$$

where V is the volume of the closed system, ΔP the difference between internal and external pressure and Δt the time interval. Connections based on KF[1]-flanges are implemented, which have a leakage rate in the order of $1 \times 10^{-9}\,\mathrm{mbar\,L\,s^{-1}}$ corresponding to a leakage rate of $1.89 \times 10^{-6}\,\mathrm{SL\,d^{-1}}$ in the LPS, which is negligible if all connections are properly made. To measure the leakage rate of the HPS, the system is filled with helium at a pressure of about 11 bar. In this measurement, the valves V_{17-20} are closed. The pressure decrease is monitored with DG_6. After six days of measurement, no significant pressure decline could be measured. For this reason, the leakage rate of the HPS is assumed to be negligible. Filling the GP with gas and closing the valves V_{21-23} allowed us to measure the leakage rate of the GP. Similarly, the pressure decline was not significant. Thus, the leakage of the GP is negligible. In addition, the LPS, HPS and GP were leak-tested with a helium leak tester[2].

The only part of our system contributing significantly to the leakage rates is the CS. In Subsection 4.1.1, the leakage of both compressors is characterized and in Subsection 4.1.2 the leakage rate of the DP_0.

4.1.1 Leakage Compressors

To evaluate the losses in the CS, helium, argon and krypton are compressed to a pressure of about 190 bar. For this purpose, the valves V_{12-17} are opened. After the system

[1] Klein-Flansch
[2] PFEIFFER VACUUM QualyTest™ Dry

Part	Volume [L]
LPS + T_0	22.2
C_0 cylinder capacity	0.32
T_1	2.04
C_1 cylinder capacity	0.101
T_2	0.075
C_1 outlet to V_{17} (except $F_{2,3}$)	0.04
F_2	0.02
F_3	0.101
GP	0.02
DP_0	$13.835 \cdot 10^{-3}$

Table 4.1: Estimated volumes for the different parts in the gas recycling system. Adapted from [24].

reaches a pressure of 200 bar, $V_{14,15}$ are closed. Thus, the compressed air supply of the compressors is cut. The pressure is monitored using DG_8 and DG_9, as shown in Figure 4.1. In a), b) and c), the pressure at DG_9 is depicted. For helium and argon, the pressure decreases rapidly until a pressure of 158 bar is reached. This specific pressure is reached for krypton at 149 bar. Subsequently, the pressure decrease reduces significantly.

Since the compressor position can not be fixed to one specific point, a likely explanation for the rapid pressure decrease, in the beginning, could be that the compressor is moving to the upper position, which causes gas expansion and reduces pressure in the cylinder, shown in Fig. 3.9. The inlet valve is entirely closed on account of the pressure gradient. However, the outlet valve is not closed completely and is, therefore, leaky. Since the atomic size of helium is significantly smaller, by a factor of ~ 3, than argon and krypton, the backflow rate for helium is larger than for argon and krypton. The rapid decrease in pressure lasts until the compressor's outlet pressure is the same as inside the cylinder. Shortly before the outlet valve opens up completely, it becomes very leaky, which explains the even higher leakage rate shortly before the kink. After the valve is opened up completely, the leakage rate is dominated by the graphite sealing at the compressor. Important to note that the first pressure drop is not an actual leak since the gas is flowing backwards into the cylinder volume and does not escape the system.

To show that the rapid pressure drop, in the beginning, comes not from an actual leak, the exact measurement as in Fig. 4.1 was repeated with helium one time, including T_2 and one time, excluding T_2 by opening and closing V_{18}, respectively. Thus, the volume of this closed system is increased by 75 cm^3. In Fig. 4.2, the results of this measurement are shown. From the starting pressures, the pressure change due to the piston movement can be calculated according to the ideal gas law in Eq. 2.22. The dashed line indicates the piston position, where 100 % means that the piston was at the lowest position and moved its complete travel range during rapid pressure drop. This pressure marks the maximum pressure drop. As our measured maximum drop is at a piston travel range of

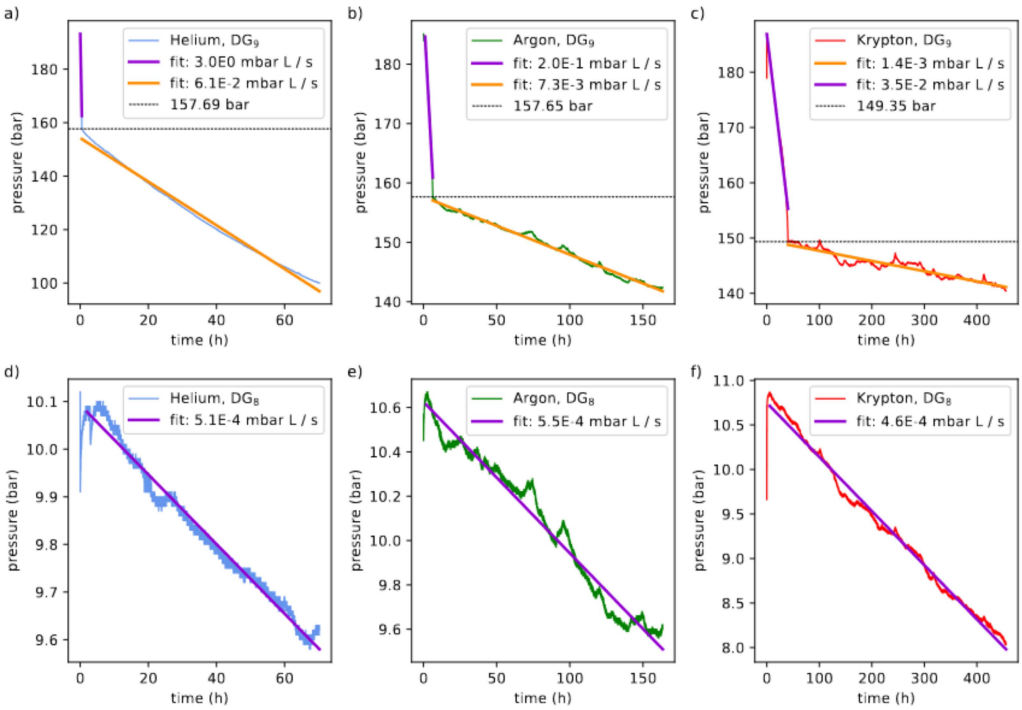

Figure 4.1: Leakage rate of the CS for helium, argon and krypton. Note the different timescales. a), b) and c) are showing the leakage rates of C_1, which were monitored at the HPS with DG_9, while d), e) and f) depict the leakage rates of C_0 at T_1 with DG_8. The pressure in a), b) and c) drops very drastically in the beginning until a certain pressure is reached (He: $158\,\mathrm{bar}$, Ar: $158\,\mathrm{bar}$, Kr: $149\,\mathrm{bar}$). Adapted from [24].

about 55 %, the rapid pressure drop can be explained through the piston movement.

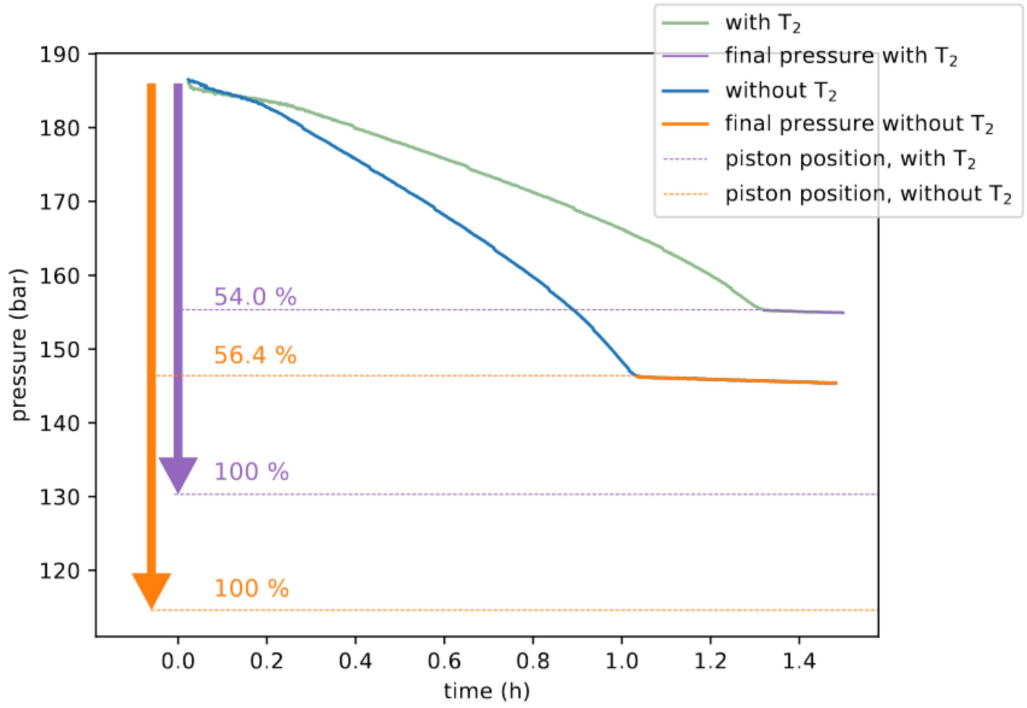

Figure 4.2: Rapid pressure drop comparison between different volumes for helium. In green, T_2 was included and in blue excluded. The final pressure is fitted linearly. From the starting pressures of both measurements (with T_2 and without T_2), the maximal possible pressure change due to the piston movement is calculated according to Eq. 2.22 and shown in the dashed purple (orange) line for the measurement including (excluding) T_2. The piston position is indicated with a dashed line. Here, 100 % means that the piston is at its upper position. The rapid pressure drop can be explained through a piston movement by 54 % (56.4 %) of the possible travel range.

Figure 4.1 a), b) and c) yield the leakage rate for C_1. Since the first rapid decrease in pressure is not an actual leak, the linear decrease after the kink is the characterizing leakage rate for C_1. For helium, argon and krypton, this rate is $q_{\mathrm{He,\,C1}} = 6.1 \times 10^{-2}\,\mathrm{mbar\,L\,s^{-1}}$, $q_{\mathrm{Ar,\,C1}} = 7.3 \times 10^{-3}\,\mathrm{mbar\,L\,s^{-1}}$ and $q_{\mathrm{Kr,\,C1}} = 1.4 \times 10^{-3}\,\mathrm{mbar\,L\,s^{-1}}$, respectively. On the contrary, Fig. 4.1 d), e) and f) give the leakage rate for C_0. The leakage rates for helium, argon and krypton are $q_{\mathrm{He,\,C0}} = 5.1 \times 10^{-4}\,\mathrm{mbar\,L\,s^{-1}}$, $q_{\mathrm{Ar,\,C0}} = 5.5 \times 10^{-4}\,\mathrm{mbar\,L\,s^{-1}}$ and $q_{\mathrm{Kr,\,C0}} = 4.6 \times 10^{-4}\,\mathrm{mbar\,L\,s^{-1}}$, respectively.

To characterize the recycling performance for argon and krypton at 55 bar, the measurement was repeated for both gases at this specific pressure. For argon, the leakage at C_1 is

Part	Gas species	Leakage rate at 200 bar ($\mathrm{mbar\,L\,s^{-1}}$)	Leakage rate at 55 ($\mathrm{mbar\,L\,s^{-1}}$)
C_0	He	5.1×10^{-4}	not measured (yet)
C_0	Ar	5.5×10^{-4}	2.2×10^{-4}
C_0	Kr	4.6×10^{-4}	1.3×10^{-4}
C_1	He	6.1×10^{-2}	not measured (yet)
C_1	Ar	7.3×10^{-3}	9.3×10^{-3}
C_1	Kr	1.4×10^{-3}	3.5×10^{-3}

Table 4.2: Summary of the leakage rates of $C_{0,1}$ for different pressures and gas species.

$q_{\mathrm{Ar,\ C1,\ 55\,bar}} = 9.3 \times 10^{-3}\,\mathrm{mbar\,L\,s^{-1}}$ and for krypton $q_{\mathrm{Kr,\ C1,\ 55\,bar}} = 3.5 \times 10^{-3}\,\mathrm{mbar\,L\,s^{-1}}$. For C_0 the leakage is given by $q_{\mathrm{Ar,\ C0,\ 55\,bar}} = 2.2 \times 10^{-4}\,\mathrm{mbar\,L\,s^{-1}}$ and $q_{\mathrm{Kr,\ C0,\ 55\,bar}} = 1.3 \times 10^{-4}\,\mathrm{mbar\,L\,s^{-1}}$. Important to note is that the pressure at DG_8 was set to 5.8 bar for the argon measurement and krypton at 7.8 bar. These pressures are also applied in the gas recycling measurements in Subsection 4.3.1 and 4.3.2. A summary of the leakage rates for the compressors at different pressures and gas species is shown in Tab. 4.2.

In Fig. 4.1, pressure fluctuations can be seen. For this reason, a temperature measurement was performed simultaneously. Figure 4.3 shows a close-up of Fig. 4.1 c) from the point on where the pressure drops slowly. At DG_9, the temperature was measured by a sensor[3] glued to the pipe. In Fig. 4.3 a), the temperature is shown. The peaks in pressure, shown in Fig. 4.3 b), correspond to the peaks in temperature. To show that the pressure fluctuation corresponds to temperature fluctuation, the pressure can be temperature corrected using the ideal gas law 2.22. For high-pressure gases ($\gg 1$ bar), the real gas model should be applied. Since it made no significant difference in the correction of pressure fluctuations, the ideal gas law was used for simplicity. Assuming that we have a constant volume V and number of particles N, yields the following expression

$$P_{\mathrm{corrected}} = P_{\mathrm{measured}} - (x \cdot (T_{\mathrm{measured}} - T_{\mathrm{mean}})), \tag{4.2}$$

where T_{mean} is the averaged temperature over the course of the measurement and $x = 0.955\,17\,\mathrm{bar\,°C^{-1}}$ is a correction factor. Figure 4.3 c) shows the corrected pressure, using Eq. 4.2. The correction factor was determined by fitting these pressure values with a linear fit and minimizing the standard deviation between the corrected pressure and the linear fit.

4.1.2 Leakage Diaphragm Pump

Another vital part of the CS is DP_0. Characterizing the leakage of DP_0 allows us to quantify the losses. For this reason, a setup for measuring the leakage rate was built, shown in Fig. 4.4. It consists of DP_0, a DG and a vacuum pump (VP). The inlet of DP_0 is sealed with a blind plug. The outlet of DP_0 is pumped by a VP. With a helium

[3] Joy-it SEN-KY15TF Sensorkit

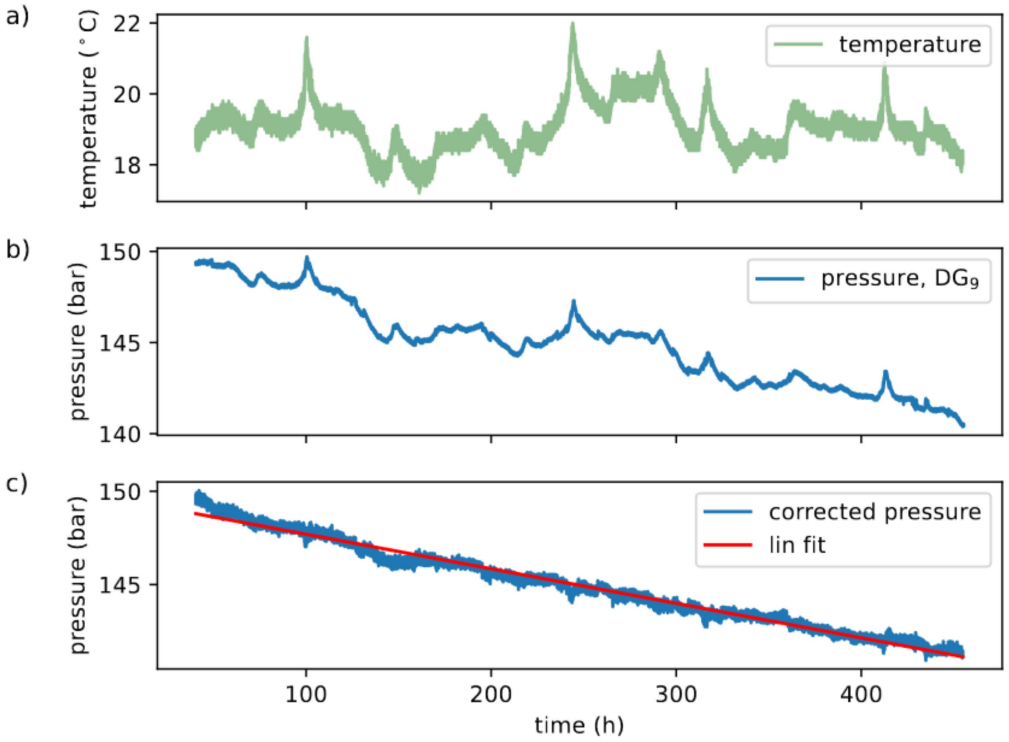

Figure 4.3: Leakage measurement of the CS, shown in b), with a simultaneous temperature measurement, shown in a). The fluctuations in pressure correspond to temperature fluctuations. In c), the pressure is corrected by these temperature fluctuations according to Eq. 4.2.

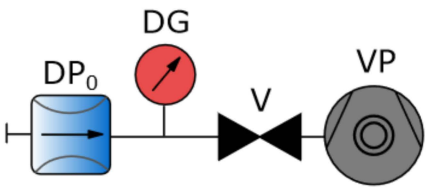

Figure 4.4: Setup for the leakage rate measurement of DP_0. The outlet of DP_0 is pumped through a vacuum pump (VP). A digital pressure gauge (DG) monitors the pressure.

leak tester[4] we made sure that there is no leak between DP_0 and VP. After the pressure at DG shows a value $< 1\,\text{mbar}$, the valve in front of the VP is closed such that the VP is not pumping DP_0 anymore. The DG monitors the pressure increase in air, leaking through DP_0. The measurement was performed one time by switching DP_0 off and starting the measurement and one time by switching it on and starting the measurement, shown in green in Fig. 4.5. The leakage rate for both states can be determined with the help of a linear fit. Hereby, only the range around 150 mbar was fitted, because 150 mbar is the specified final pressure for DP_0. For the off-switched DP_0, the leakage rate is $q_{\text{off}} = 1.83 \times 10^{-2}\,\text{mbar}\,\text{L}\,\text{s}^{-1}$ and for the on-switched DP_0, $q_{\text{on}} = 1.69 \times 10^{-2}\,\text{mbar}\,\text{L}\,\text{s}^{-1}$.

To improve the leakage rate, every sealing was covered with vacuum-compatible silicon grease[5]. The exact measurement was repeated with this improved DP_0. The results are shown in blue in Fig. 4.5. The leakage rate for the off-switched state is $q_{\text{off, improved}} = 1.45 \times 10^{-2}\,\text{mbar}\,\text{L}\,\text{s}^{-1}$ and for the on-switched state $q_{\text{on, improved}} = 1.01 \times 10^{-2}\,\text{mbar}\,\text{L}\,\text{s}^{-1}$. The improved version in the on-switched state is, therefore better with a factor of 1.7 and for the off-switched state, 1.3. A summary of the measured leakage rates is shown in Tab. 4.3.

State	Mode	Leakage rate ($\text{mbar}\,\text{L}\,\text{s}^{-1}$)
On	Without silicon grease	1.69×10^{-2}
Off	Without silicon grease	1.83×10^{-2}
On	With silicon grease	1.01×10^{-2}
Off	With silicon grease	1.45×10^{-2}

Table 4.3: Summary of the leakage rates of DP_0.

[4] PFEIFFER VACUUM QualyTest™ Dry
[5] DOW CORNING high vacuum grease

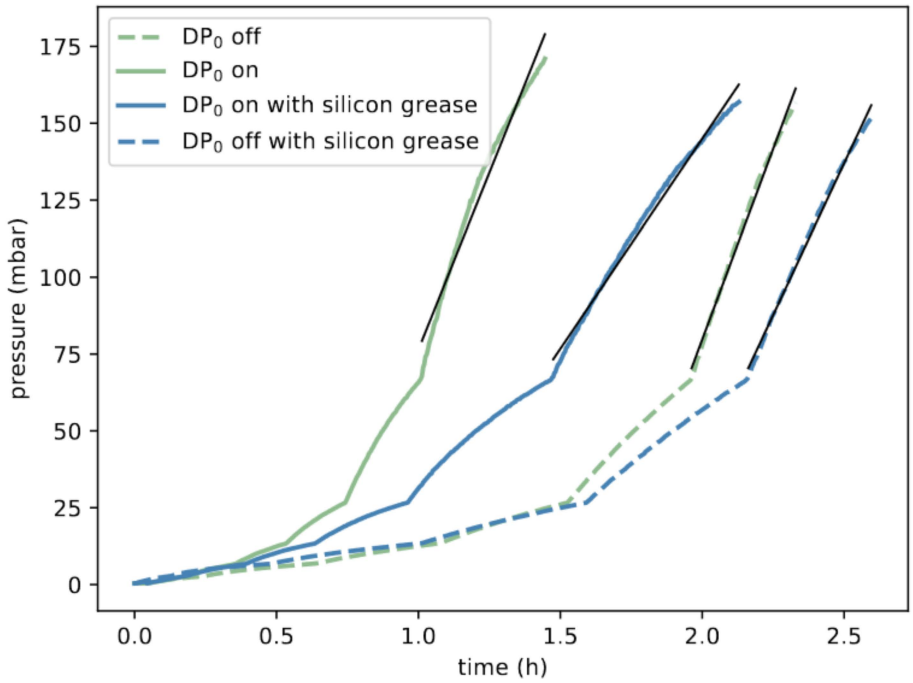

Figure 4.5: Leakage rate of DP_0 with and without silicon grease. The leakage rate for DP_0 is shown in green. Sealing DP_0 with silicon grease and rubber improves the leakage rate, which is shown in blue. The rates were measured for the off-switched state, dashed line, and on-switched state, continuous line. A slower pressure rise indicates a reduced leakage rate.

4.2 Nozzle Consumption

An essential parameter for the characterization of the total gas recycling efficiency is the nozzle consumption, which describes the amount of gas that flows through the nozzle in a certain time interval. The nozzle consumption varies greatly, depending on different factors such as the diameter of the nozzle, the gas species and the gas pressure. The larger the diameter, the greater the consumption. Another factor is the pressure at which the nozzle is operated. This so-called backing pressure can be regulated through PR_3. The higher the backing pressure, the greater the nozzle consumption. These factors are further investigated in Subsections 4.2.1 and 4.2.2.

4.2.1 Consumption for various Nozzle Sizes

To compare the nozzle consumption for three different nozzle diameters, the different nozzles are introduced in the following. The first nozzle, "nozzle 1", had visible black spots on the surface, presumably caused by the high intensity of the laser. With a microscope [6], nozzle 1 was further investigated. The results are shown in Fig. 4.6. Three main observations can be drawn from this. One, the black spots, which were also visible to the eye can also be seen on a microscope scale, see Fig. 4.6 b). Two, the diameter of nozzle 1 is approximately $d_1 = 28\,\mu\text{m}$, see Fig. 4.6 c). Three, light from a source placed below the nozzle cannot pass through the aperture without interference. These findings suggest that the gas flow is unintentionally affected.

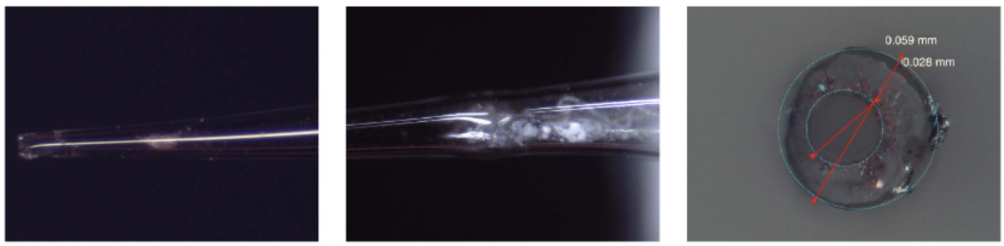

(a) Side view. (b) Side view. (c) Top view.

Figure 4.6: Microscope pictures of nozzle 1. a) shows the side profile. In b) a close-up of a) is shown, where the black spots are visible. c) depicts the top view of nozzle 1. From c), the diameter could be determined to approximately $d_1 = 28\,\mu\text{m}$.

Because nozzle 1 seems unsuitable for further use, two other nozzles were investigated under the microscope. The so-called "nozzle 2" is depicted in Fig. 4.7. With the microscope, it was possible to determine the diameter of the nozzle to $d_2 = 40\,\mu\text{m}$. Nozzle 2 is now implemented in our gas recycling system and used in the gas recycling measurements in Section 4.3.

[6] KEYENCE VHX-7000

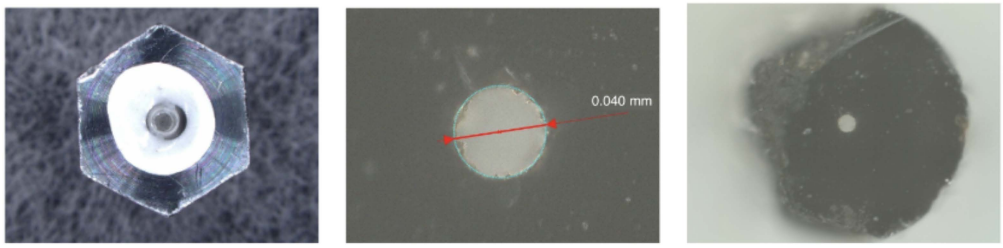

(a) Top view. (b) Top view. (c) Top view.

Figure 4.7: Microscope pictures of nozzle 2. In a) nozzle is shown from the top. The nozzle is glued in an aluminum mount. The inner diameter of nozzle two is approximately $d_2 = 40\,\mu\text{m}$ (b)). In c) inner and outer diameters of nozzle 2 can be seen.

The third nozzle, "nozzle 3", is shown in Fig. 4.8. On a micrometer scale, it was possible to see that nozzle 3 has a broken tip, see Fig. 4.8a),b). The diameter of nozzle 3 is approximately $d_3 = 100\,\mu\text{m}$. With a broken tip, it is unclear how gas flows into the differential pump system. It would be possible that the gas is divergent and is not entering the first stage correctly. Therefore, nozzle 3 was not implemented for the gas recycling measurements in Section 4.3.

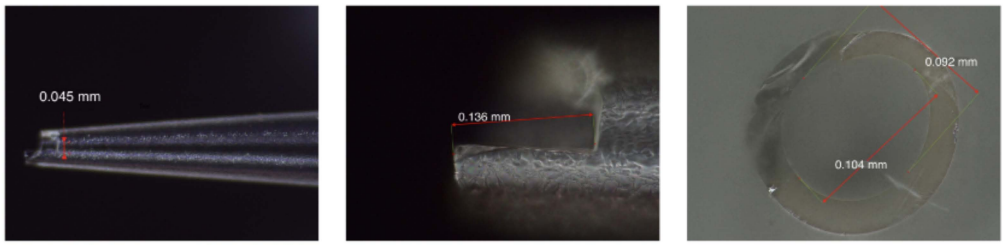

(a) Side view. (b) Side view. (c) Top view.

Figure 4.8: Microscope pictures of nozzle 3. In a), nozzle 3 is shown from the side. At the tip of the nozzle, a part is broken off. This can be seen in a close-up in b). In c), the inner and outer diameter of nozzle 3 is shown.

The nozzle consumption was measured to compare the performances of the three different nozzle sizes. For this purpose, T_2 was filled with argon to 100 bar. This can be achieved by opening the valves $V_{10,11,13,16-18,20}$. After T_2 is filled up, V_{17} is closed again and valve V_{23} towards the gas nozzle is opened. Therefore, the nozzle consumes a defined volume of T_2 and one meter of a 1/8" tube. With PR_3, the backing pressure is regulated to 20 bar. Due to this constant output rate, the flow rate remains the same. Therefore, a linear decrease at T_2 is expected as long as the pressure at T_2 remains significantly higher than at the nozzle. The nozzle consumption was measured for the three different nozzle sizes at 20 bar backing pressure. The result is shown in Fig. 4.2.1. The consumption of nozzle

1 to 3 are $q_{nc,\,1} = 2.46\,\mathrm{mbar\,L\,s^{-1}}$, $q_{nc,\,2} = 2.50\,\mathrm{mbar\,L\,s^{-1}}$ and $q_{nc,\,3} = 64.29\,\mathrm{mbar\,L\,s^{-1}}$, respectively. As expected, $q_{nc,\,1} < q_{nc,\,2} < q_{nc,\,3}$.

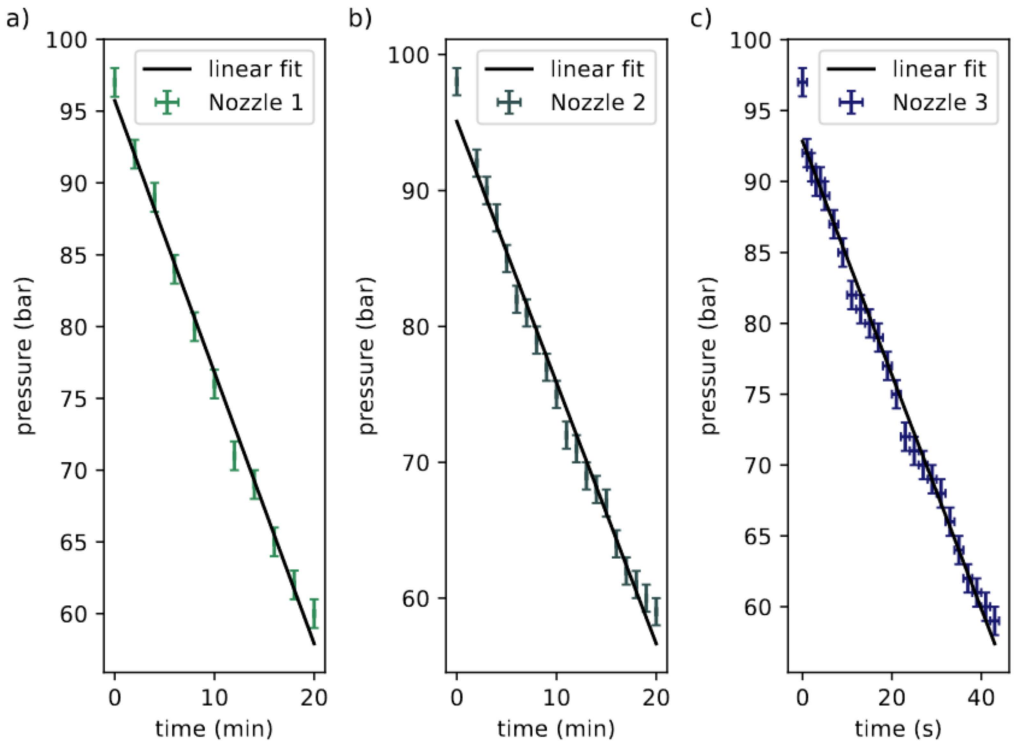

Figure 4.9: Nozzle consumption for three different nozzle sizes at a backing pressure of 20 bar. In a), nozzle 1 consumption with a diameter of $d_1 = 28\,\mu\mathrm{m}$. In b), the nozzle 2 consumption is shown with a diameter of $d_2 = 40\,\mu\mathrm{m}$. In c), nozzle 3 with a diameter of $100\,\mu\mathrm{m}$ was used. Note the different timescale in c).

4.2.2 Consumption for different Gases

The nozzle consumption was measured again at a backing pressure of 10 bar, which is the pressure used in the gas recycling measurements in Section 4.3. This time, the nozzle consumption of nozzle 2 was measured for argon and krypton, as shown in Fig. 4.10. The nozzle consumption for argon hereby is $q_{nc,\,ar} = 1.48\,\mathrm{mbar\,L\,s^{-1}}$ and for krypton $q_{nc,\,kr} = 0.89\,\mathrm{mbar\,L\,s^{-1}}$. This means that the nozzle consumption for krypton is lower than for argon. The molecular weight of gas seems to be the decisive factor for a different gas consumption since all other quantities in the measurement such as temperature and backing pressure are assumed to be equal. As argon is ~ 2 times lighter than krypton, less energy by a factor of ~ 1.5 is required to accelerate it to the same gas velocity, see

Eq. 2.18. This means that less gas would need to be supplied through the nozzle per unit of time to achieve the same mass flow rate as krypton. Therefore, the nozzle consumption for argon is lower by a factor of 1.66 than for krypton, which is close to the gas velocity factor. A summary of the different nozzle consumption measurements is shown in Tab. 4.4.

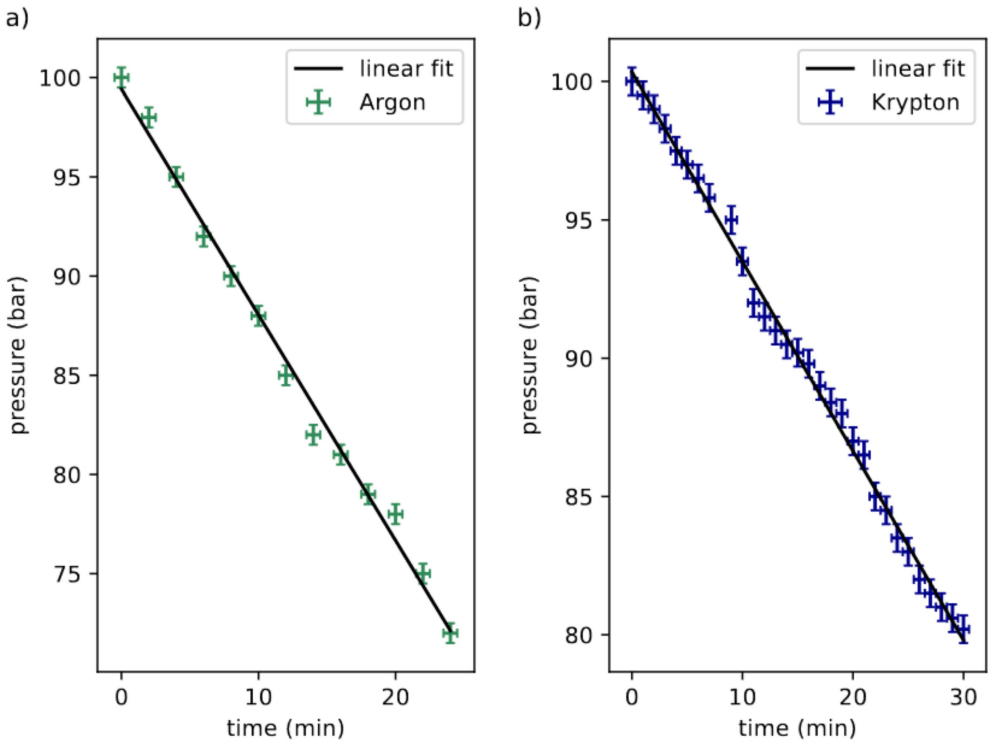

Figure 4.10: Nozzle 2 consumption for argon and krypton at a backing pressure of 10 bar. In a) T_2 was filled with argon. In b) T_2 was filled with krypton. Note the different timescales. The nozzle consumption for argon is higher by a factor of ~ 1.66 than for krypton.

Nozzle	Size (µm)	Gas species	Backing pressure (bar)	Consumption (mbar L s^{-1})
1	28	Argon	20	2.46
2	40	Argon	20	2.50
3	100	Argon	20	64.29
2	40	Argon	10	1.48
2	40	Krypton	10	0.89

Table 4.4: Summary of the nozzle consumption measurements for different gas species, nozzle sizes and backing pressures.

4.3 Gas Recycling

To assess the recycling efficiency of the system, gas recycling measurements were performed over several days. Due to costs and availability, argon and krypton were used in these measurements. To remove the gas from previous use, the system needs to be flushed and pumped with the target before starting gas recycling measurements to decrease air and water contamination.

After cleaning the system, it is filled with gas by opening $V_{10,11,13-18,20,21,23}$. The gas is compressed in the CS by regulating the CAS with PR_1 and PR_2. The gas recycling measurements for argon and krypton were carried out with a backing pressure of 10 bar. This pressure was set through PR_3 and monitoring the pressure at DG_{10}. The backing pressure was limited due to the use of the mass spectrometer, which requires a vacuum environment below 1×10^{-5} mbar. The pressure at T_1 was set to about 8 bar. Figure 4.11 shows an overview of how the valves are set in the following measurements. The red line indicates the gas flow. Because DG_6 was not working correctly, especially for low pressures, AG_2 was used to monitor the pressure at the LPS. For this purpose, a camera imaged the gauge and with software, the images were converted to pressure values.

The recycling efficiency was investigated for two gas species and two different pressures at the CS outlet. Subsection 4.3.1 discusses the recycling rate for argon at a pressure of 55 bar and Subsection 4.3.2 examines the same measurement for krypton. In Subsection 4.3.3, argon is recycled at a pressure of 100 bar. Additionally, a recycling comparison with all TMPs and only using the differential pumping system is discussed.

4.3.1 Recycling Argon at 55 bar

For a first measurement, argon was recycled and the output pressure of the CS was set to ~ 55 bar. The recycling performance is shown in Fig. 4.12. The CS outlet and the backing pressure at the nozzle are staying constant over time, as shown in Fig. 4.12 b). However, the pressure at the LPS declines over time, Fig. 4.12 a). This decline was fitted linearly since the LPS is supplied with a constant nozzle backing pressure. The fit yields a leakage rate of $3.7 \times 10^{-2}\,\mathrm{mbar\,L\,s^{-1}}$, corresponding to a consumption of $3.15\,\mathrm{SL\,d^{-1}}$. This indicates that the system needs to be refilled every three days with $\sim$ 9 SL of gas to ensure a continuous gas supply. Because the nozzle consumption at 10 bar backing pressure is $\sim 130\,\mathrm{SL\,d^{-1}}$, a recycling rate of $\sim 98\,\%$ is achieved. In Fig. 4.12 c), the partial pressures inside the main chamber are shown. Water contamination is very low, in the order of 10^{-9} mbar, since F_1 filters water out of the system. The partial pressure of argon stays constant at the order of 10^{-5} mbar over time. At the end of the measurement, the nitrogen level concentration in the chamber rises slightly. This could be due to a small leak in the system over time due to the vibration of pumps. The number of hydrocarbons C_nH_{2n+2} stays constant throughout the measurement.

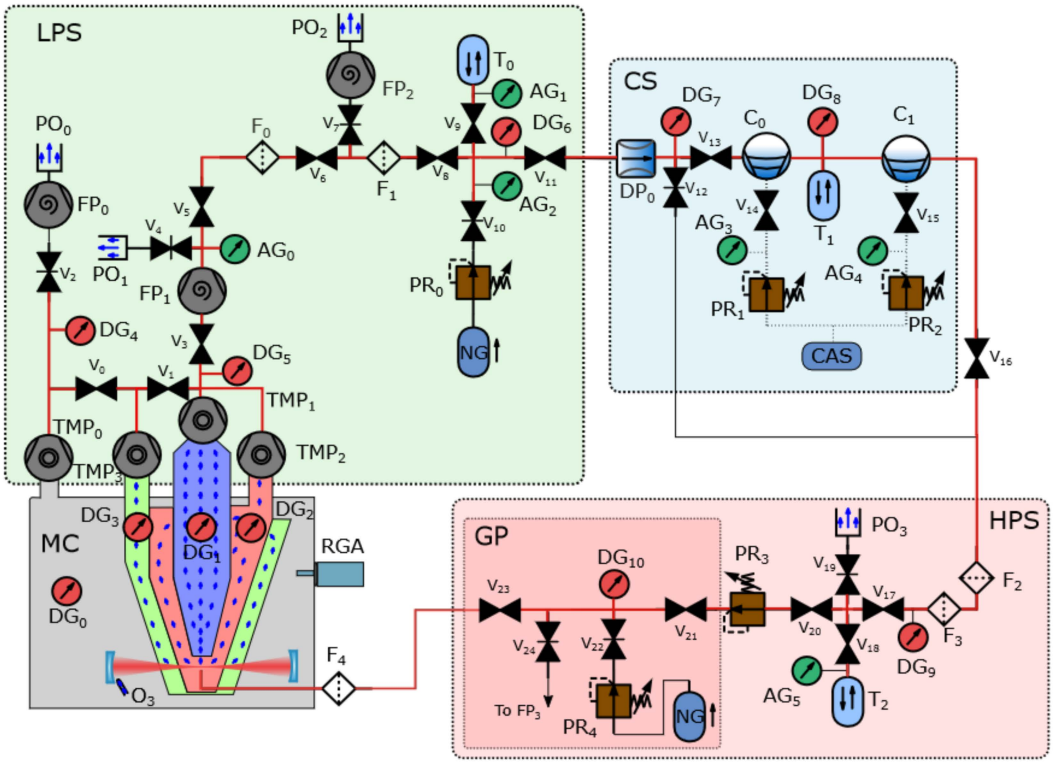

Figure 4.11: Gas flow chart used for the measurements in Fig. 4.12 and Fig. 4.13, where all TMPs are recycling the gas. The gas flow in these measurements is indicated in red. Bars in valves denote closed valves. Valves with no bars are opened.

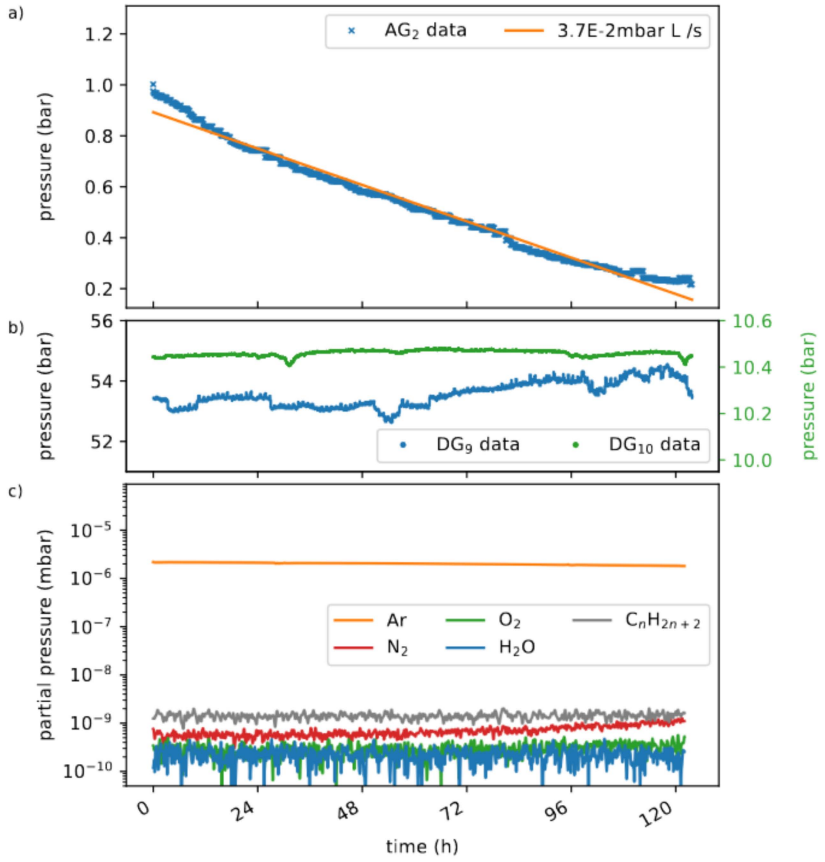

Figure 4.12: Recycling argon at $\sim 55\,\mathrm{bar}$ with a backing pressure of $\sim 10\,\mathrm{bar}$. The system empties after about five days. In a), the pressure at the LPS is shown. A linear fit yields the leakage rate of the total gas recycling system. The pressure at HPS (blue) and GP (green) stays constant, shown in b). In c), the residual gas partial pressures in the MC are shown. The contamination level stays low. Nitrogen is rising slightly at the end of the measurement, indicating that air slowly leaks into the system.

4.3.2 Recycling Krypton at 55 bar

The exact measurement as in Subsection 4.3.1 was performed for krypton again. The result is shown in Fig. 4.13. The leakage rate of the system is shown in Fig. 4.13 a) and consists of two regimes i) time $< 29\,\mathrm{hours}$ and ii) time $> 29\,\mathrm{hours}$. Linear fits yield leakage rates of $8.0 \times 10^{-2}\,\mathrm{mbar\,L\,s^{-1}}$ and $2.0 \times 10^{-2}\,\mathrm{mbar\,L\,s^{-1}}$ corresponding to a consumption of $6.82\,\mathrm{SL\,d^{-1}}$ and $1.71\,\mathrm{SL\,d^{-1}}$ for the first and second regime, respectively. With a nozzle consumption of $\sim 76\,\mathrm{SL\,d^{-1}}$ this yields a recycling rate of $\sim 91\,\%$ and $\sim 98\,\%$ for regime i) and ii), respectively. Similar regimes were found at $\mathrm{DG_7}$ and the compressor frequency

of C_0, see Fig. 4.14. The compressor beat frequency is shown in blue and the decreasing pressure at the LPS in orange. In regime i), the compressor beat frequency is about 3.6 beats per hour. This low beat frequency causes gas and therefore pressure, to build up between the LPS and the compressor. If the compressor beats, the pressure at the LPS decreases rapidly and subsequently increases again due to the pressure build-up. This explains the comparably strong pressure oscillations at the beginning of the measurement. Nonetheless, an explanation for the rapid pressure decrease in the beginning is unclear and needs to be further investigated. Figure 4.14 shows the dependency of the compressor beat frequency on the pressure decrease at the LPS, which was measured simultaneously with the measurement in Fig. 4.3.2. The beat frequency correlates directly with the pressure value. The higher the pressure, the lower the compressor beat frequency, which is shown in the two close-ups of the pressure. The minima correspond to one compressor beat. For pressures under 150 mbar, the compressor beat frequency increases significantly. Due to the compressor wear at such high frequencies, it is not possible to operate the gas recycling system at a pressure below 150 mbar at the LPS. That is why the gas recycling measurements were stopped at the time, where the LPS reached a pressure of about 150 mbar.

Figure 4.13 b) shows that the CS outlet is roughly staying constant while the backing pressure decreases over time. As the CS outlet pressure is staying constant, a likely explanation for the decreasing backing pressure is that PR_3 is not reliable for long-term operation. In Fig. 4.13 c), the partial pressure of krypton is decreasing due to the decreasing backing pressure in b). Another observation is the increase of nitrogen by 46 % and oxygen concentration in the chamber. Air seems to be coming into the system. One possibility is that KF-connections slowly loosened over the course of the measurement series (first, argon at 100 bar was measured [23], then argon at 55 bar and finally, krypton at 55 bar without tightening the connections). The water and hydrocarbon contamination stays constant at the order of 1×10^{-10} mbar and 1×10^{-9} mbar, respectively.

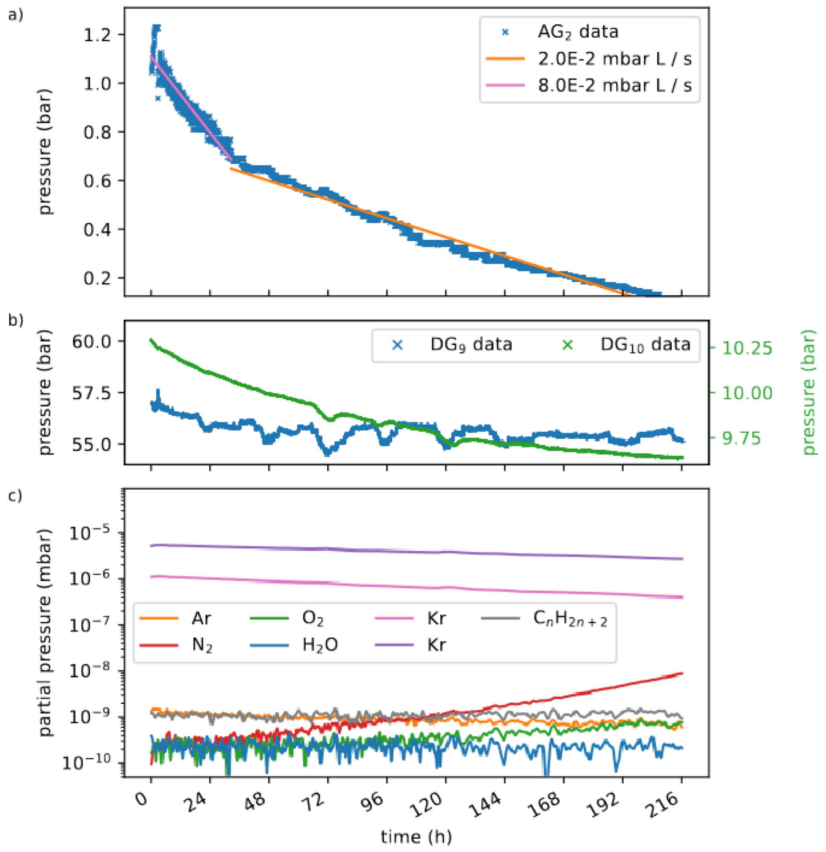

Figure 4.13: Recycling krypton at approximately $55\,\mathrm{bar}$ with a backing pressure of $10\,\mathrm{bar}$. The measurement lasted for a bit more than nine days. The pressure at LPS drops linearly, shown in a), yielding the leaking rate of the system. In b), the pressure at the HPS (blue) and GP (green) is shown. The backing pressure is decreasing over time. In c), the residual gases in the MC are depicted. The amount of krypton decreases slowly over time, which could be due to the decreasing nozzle backing pressure. Nitrogen and oxygen are rising significantly, indicating a leak.

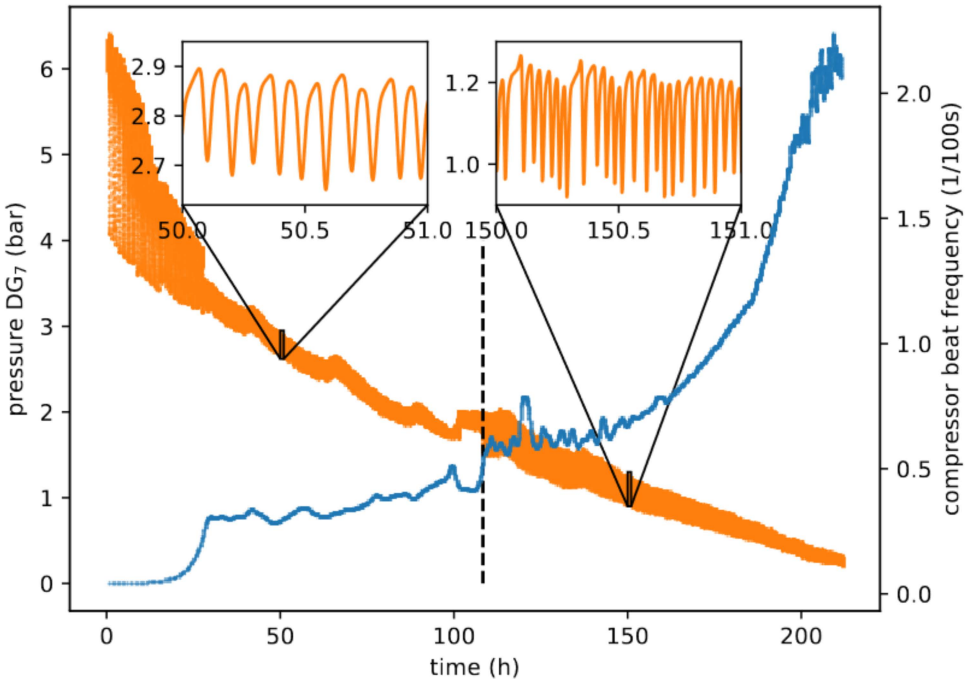

Figure 4.14: Compressor beat frequency dependence on the pressure decrease at the LPS. The higher the pressure, shown in orange, the lower the compressor beat frequency, shown in blue. The black dashed line indicates the boundary, where another Gaussian filter was used for the compressor beat frequency analysis.

4.3.3 Recycling Argon at 100 bar

It is also possible to recycle the target gas with the differential pumping system only, excluding the exhaust of the MC, by closing valve V_0 and opening V_2. This set of valves was employed from the beginning of the measurement until $\sim 160\,\mathrm{h}$, as indicated by the grey dashed line in Fig. 4.15. After the grey line, the valves were set as in the previous measurements, recycling with all TMPs. While generating HH, ozone is injected into the MC and TMP_0 is flushed with nitrogen. Since we aim to recycle only the target gas, switching between these two recycling modes is beneficial. No significant difference in the leaking rates between the full recycling mode and the differential pumping mode can be determined, which is due to the significantly lower gas volume by a factor of ~ 1000 in TMP_0. As the main loss in our system is the CS, higher pressures lead to an increased leakage rate. The system had to be refilled, as indicated with "R", approximately every two days with 14 SL of argon to guarantee a continuous flow of gas. To refill the system,

the valves $V_{8,11}$ are closed and $V_{9,10}$ are opened. After the LPS reaches a pressure near 1 bar, V_{10} is closed again and V_{11} is opened to ensure that the gas is not flowing backwards. After the pressure values, monitored at AG_0 and AG_1 are similar, the system can be refilled again, until a pressure of 1 bar is reached at AG_1. Fitting the linear decrease at the LPS in Fig. 4.15 a), yields a leaking rate of $\sim 7.9 \times 10^{-2}\,\mathrm{mbar\,L\,s^{-1}}$, which corresponds to a loss of $\sim 6.8\,\mathrm{SL\,d^{-1}}$. Since different end pressures are present at the LPS, the linear fits are not comparable to one another. With a nozzle consumption of $\sim 130\,\mathrm{SL\,d^{-1}}$, this signifies a recycling rate of $\sim 95\,\%$. Figure 4.15 b), shows that the CS outlet pressure decreases slowly over time as well as the backing pressure at the nozzle. With a decrease in the backing pressure, the argon partial pressure decreases as well, as shown in Fig. 4.15 c). The partial pressures of hydrocarbons, nitrogen and oxygen are roughly staying constant. The water contamination, which was high in the beginning because the measurement was started approximately three hours after the MC was closed after construction work, reduces significantly in the two first days of the measurement, indicating that the adsorption trap filter in the system works well. To quantify this further, 60 h after the beginning of the measurement, the filter approaches the asymptotic limit. With 50 SL of gas in the system and a consumption of $130\,\mathrm{SL\,d^{-1}}$, this corresponds to 6.5 filter runs until the filter is at its limit and water contamination in the order of $1 \times 10^{-10}\,\mathrm{mbar}$ is present. The reason for the high water contamination at the beginning of the measurement was the chamber opening four hours before starting the recycling measurement. A summary of the different gas recycling measurements is given in Tab. 4.5.

Gas species	CS outlet pressure (bar)	Leakage rate ($\mathrm{mbar\,L\,s^{-1}}$)	Recycling rate (%)
Argon	55	3.7×10^{-2}	98
Krypton	55	2.0×10^{-2}	98
Argon	105	7.9×10^{-2}	95

Table 4.5: Summary of the different gas recycling measurements.

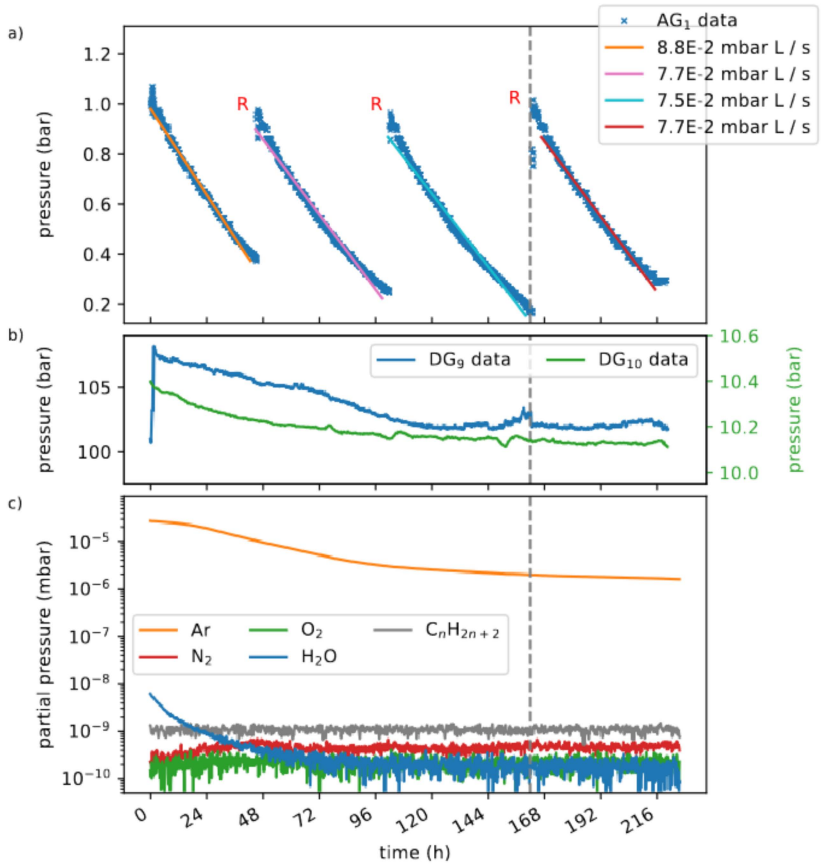

Figure 4.15: Recycling argon with approximately 105 bar. The backing pressure for the nozzle was set to 10 bar. In a), the pressure at the LPS is shown. The system was refilled, as indicated with "R", every two days to ensure a continuous operation with $\sim 20\,\mathrm{SL}$ of argon. In b), the pressure at the HPS (in blue) and gas nozzle (in green) is shown. They decrease over time. c) The argon partial pressure decreases as well since the backing pressure decreases. The water contamination in the system reduces significantly, because of the employed filters. The amount of hydrocarbons, nitrogen and oxygen is roughly staying constant. Two recycling modes were applied in this measurement. First, recycling with TMP_{1-3}, and after 160 h, as indicated by the grey dashed line, recycling with all TMPs. Adapted from [24].

5 Conclusion and Outlook

A closed-loop noble gas recycling system was commissioned to ensure continuous operation for high repetition rate HHG, enabling long spectroscopy measurements within the XUV region in the order of weeks. The target gas is injected close to the laser focus by a 40 µm nozzle and caught by a differential pumping system, avoiding multiple interactions of a single atom of the target gas with the laser pulses. The gas is cleaned by several filters, compressed up to a pressure of 200 bar and then injected back into the vacuum chamber.

Characterization of the leakage in the closed-loop system showed that the main leak comes from the compressor station, where the leakage rate of its compressor components was further investigated. Sealing the diaphragm pump with silicon grease and rubber improved the incoming air leakage from $1.69 \times 10^{-2}\,\mathrm{mbar\,L\,s^{-1}}$ to $1.01 \times 10^{-2}\,\mathrm{mbar\,L\,s^{-1}}$. A new diaphragm pump with a specified helium leakage rate of $6 \times 10^{-6}\,\mathrm{mbar\,L\,s^{-1}}$ will be installed soon. This will probably improve the gas recycling efficiency significantly since the compressors, which are the major loss source, can be skipped if the gas needs to be recompressed to a few bar only.

The amount of gas that flows through the nozzle over a time period is a crucial parameter to describe the gas recycling rate. The nozzle consumption was measured for three different nozzle diameters and different backing pressures. For a backing pressure of 10 bar and argon as a target gas, this measurement yielded a consumption of about 130 SL per day. Using krypton as a target gas, the 40 µm diameter nozzle consumed about 80 SL per day.

With a recycling rate of $\sim 98\,\%$ and at a compression up to 55 bar, the measurement ran continuously without refill for nine days (five days) for krypton (argon). Recycling argon with a pressure of ~ 100 bar increased the leakage rate slightly and required filling the system every two days with ~ 20 SL of gas. The nozzle backing pressure was set to 10 bar. The water contamination stayed below 2×10^{-9} mbar throughout the measurement, while nitrogen and oxygen increased, probably because of a leak. This system efficiently saves more than 127 SL of argon per day. Recycling krypton saves 74 SL per day. This recycling rate allows for saving costs of several thousand euros per day using xenon as a target gas. It was shown that the system can run in two recycling modes: recycling the gas with all turbomolecular pumps and recycling the gas with the differential pumping system only. The system runs in continuous closed-loop operation. Depending on the pressure set at the compressor station outlet, it requires filling the noble gas recycling system with a

defined amount of gas every two to nine days.

The nozzle backing pressure was limited by using the mass spectrometer, which requires operation in a vacuum environment below 10^{-5} mbar. Since the injection of gas deteriorates the vacuum conditions, the backing pressure set in the gas recycling measurements was limited to ~ 10 bar. However, the nozzle can be operated at higher backing pressure (> 10 bar) without using the mass spectrometer to ensure continuous phase-matched XUV frequency comb operation.

To test the closed-loop noble gas recycling system even further, the efficiency of XUV light generation together with the gas recycling system will be probed. As ozone is injected into the chamber to prevent the mirrors from degradation, it is interesting how this injection affects the gas recycling performance and will be tested soon.

Acronyms

ADC	analog-to-digital converter. 26
ADK	Ammosov-Delone-Krainov. 11
AG	analog pressure gauge. 23
C	compressor. 23
CAS	compressed air supply. 23, 29, 30, 43
CM	curved mirror. 18, 20, 21
CryPTex-SC	superconduction Paul trap. 1, 2, 20
CS	compressor station. 22, 23, 25, 31, 33, 35, 36, 43, 46, 48, 49
DG	digital pressure gauge. 23, 35, 37
DP	diaphragm pump. 23, 25
EBIT	electron beam ion trap. 1
F	filter. 23
FP	fore-vacuum pump. 23
FPM	piezo-driven flat cavity mirror. 18, 20
FR	flow regulator. 21
fsEC	femtosecond enhancement cavity. 17–21
FWHM	full-width at half-maximum. 10
GM	grating mirror. 18–21
GP	gas panel. 19, 23, 26, 31, 45, 47
HCI	highly charged ion. 1, 2, 5
HEPA	high-efficiency particulate absorbing. 27
HH	high harmonics. 1, 5, 6, 17–22, 48
HHG	high harmonic generation. 1, 2, 5–10, 19, 20, 22, 25, 51
HPS	high-pressure system. 22, 23, 25, 26, 31, 33, 45, 47, 50
IC	input coupler. 18, 20, 21
IR	infrared. 5
LPS	low-pressure system. 22, 23, 25, 31, 43, 45–50
MC	main chamber. 20, 21, 23, 25, 45, 47–49
NIR	near-infrared. 1, 2, 18
NV	needle valve. 21
OC	ozone catalyst. 21
PO	pressure outlet. 23

PR	pressure regulator. 23
RGA	residual gas analyzer. 23, 28, 29
SL	standard liter. 14
T	storage/buffer tank. 23
TMP	turbomolecular pump. 17, 20, 23, 43, 44, 48
UHV	ultra-high vacuum. 20
UV	ultraviolet. 5
V	valve. 23
VP	vacuum pump. 35, 37
XUV	extreme ultraviolet. 1, 2, 5, 10, 19, 20, 51, 52

Bibliography

[1] P. A. Zyla et al., "Review of particle physics", Progress of Theoretical and Experimental Physics **2020**, 1–2093 (2020).

[2] M. Dine and A. Kusenko, "Origin of the matter-antimatter asymmetry", Rev. Mod. Phys. **76**, 1–30 (2004).

[3] T. Harko, P. Liang, and S.-D. Liang, "Non-baryonic dark matter: observational evidence and detection methods", Rep. Prog. Phys **63**, 793 (2000).

[4] P. J. E. Peebles and B. Ratra, "The cosmological constant and dark energy", arXiv **0207347** (2002).

[5] A. Einstein, *Die Feldgleichungen der Gravitation* (Springer Berlin Heidelberg, 1915), pp. 137–141.

[6] J.-P. Uzan, "Varying constants, gravitation and cosmology", `10.12942/lrr-2011-2` (2010).

[7] S. A. King, L. J. Spieß, P. Micke, A. Wilzewski, T. Leopold, E. Benkler, R. Lange, N. Huntemann, A. Surzhykov, V. A. Yerokhin, J. R. Crespo López-Urrutia, and P. O. Schmidt, "An optical atomic clock based on a highly charged ion", Nature **611**, 43–47 (2022).

[8] J. Nauta, "An extreme-ultraviolet frequency comb enabling frequency metrology with highly charged ions", PhD thesis (Ruprecht-Karls-Universität Heidelberg, 2020).

[9] A. Cingöz, D. C. Yost, T. K. Allison, A. Ruehl, M. E. Fermann, I. Hartl, and J. Ye, "Direct frequency comb spectroscopy in the extreme ultraviolet", Nature **482**, 68–71 (2012).

[10] J. Nauta, J.-H. Oelmann, A. Borodin, A. Ackermann, P. Knauer, I. S. Muhammad, R. Pappenberger, T. Pfeifer, and J. R. Crespo López-Urrutia, "XUV frequency comb production with an astigmatism-compensated enhancement cavity", Optics Express **29**, 2624 (2021).

[11] M. A. Levine, R. E. Marrs, J. R. Henderson, D. A. Knapp, and M. B. Schneider, "The electron beam ion trap: a new instrument for atomic physics measurements", Physica Scripta **22**, 157–163 (1988).

[12] J. Stark, C. Warnecke, S. Bogen, S. Chen, E. A. Dijck, S. Kühn, M. K. Rosner, A. Graf, J. Nauta, J.-H. Oelmann, L. Schmöger, M. Schwarz, D. Liebert, L. J. Spieß, S. A. King, T. Leopold, P. Micke, P. O. Schmidt, T. Pfeifer, and J. R. Crespo López-Urrutia, "An ultralow-noise superconducting radio-frequency ion trap for frequency metrology with highly charged ions", Review of Scientific Instruments **92**, 083203 (2021).

[13] P. Schmidt, T. Rosenband, C. Langer, W. M. Itano, J. C. Bergquist, and D. J. Wineland, "Spectroscopy using quantum logic", Science **309**, 746–749 (2005).

[14] M. Ferray, A. L'Huillier, X. F. Li, L. A. Lompré, G. Mainfray, and C. Manus, "Multiple-harmonic conversion of 1064 nm radiation in rare gases", Journal of Physics B: Atomic, Molecular and Optical Physics (1988).

[15] C. J. Berganza and J. H. Zhang, "The role of helium gas in medicine", Medical Gas Research **3**, 18 (2013).

[16] E. Esencan, S. Yuksel, Y. B. Tosun, A. Robinot, I. Solaroglu, and J. H. Zhang, "Xenon in medical area: emphasis on neuroprotection in hypoxia and anesthesia", Medical Gas Research **3**, 4 (2013).

[17] J. Tušek and M. Suban, "Experimental research of the effect of hydrogen in argon as a shielding gas in arc welding of high-alloy stainless steel", International Journal of Hydrogen Energy **25**, 369–376 (2000).

[18] B. A. Glowacki, W. J. Nuttall, and R. H. Clarke, "Beyond the Helium Conundrum", IEEE Transactions on Applied Superconductivity **23** (2013).

[19] M. Schumann, "Dark matter search with liquid noble gases", arXiv **1206.2169** (2012).

[20] S. Yuji, B. Marty, and P. Burnard, *The noble gases as geochemical tracers* (Springer Berlin Heidelberg, Jan. 2013), pp. 17–31.

[21] C. T. Chiang, M. Huth, A. Trützschler, F. O. Schumann, J. Kirschner, and W. Widdra, "Efficient and tunable high-order harmonic light sources for photoelectron spectroscopy at surfaces", Journal of Electron Spectroscopy and Related Phenomena **200**, 15–21 (2015).

[22] R. Wallauer, J. Reimann, N. Armbrust, J. Güdde, and U. Höfer, "Intervalley scattering in MoS2 imaged by two-photon photoemission with a high-harmonic probe", Applied Physics Letters **109**, 10.1063/1.4965839 (2016).

[23] J.-H. Oelmann, L. Guth, T. Heldt, N. Griesbach, R. Hector, N. Lackmann, J. Nauta, T. Pfeifer, and J. R. Crespo López-Urrutia, "Closed-cycle noble gas recycling system for high-repetition rate high-harmonic generation", (In preperation).

[24] J.-H. Oelmann, "Highly nonlinear light-matter interaction using cavity-enhanced frequency combs", PhD thesis (Ruprecht-Karls-Universität Heidelberg, 2023).

[25] R. C. Hector, "Characterization of a Xenon-Recycling-System for an Extreme-Ultraviolet Frequency Comb" (Ruprecht-Karls-Universität Heidelberg, 2022).

[26] A. Cingoz, D. Yost, T. Allison, A. Ruehl, M. Fermann, I. Hartl, and J. Ye, "Direct frequency comb spectroscopy in the extreme ultraviolet", Nature **482**, 68–71 (2012).

[27] M. Zürch, S. Foertsch, M. Matzas, K. Pachmann, R. Kuth, and C. Spielmann, "Cancer cell classification with coherent diffraction imaging using an extreme ultraviolet radiation source", Journal of Medical Imaging **1**, 031008 (2014).

[28] M. Lewenstein, P. Balcou, M. Y. Ivanov, A. L'Huillier, and P. B. Corkum, "Theory of high-harmonic generation by low-frequency laser fields", Phys. Rev. A **49**, 2117–2132 (1994).

[29] P. B. Corkum, "Plasma Perspective on Strong-Field Multiphoton Ionization", Physical Review Letters **71**, 1994–1997 (1993).

[30] M. Grishin, *Advances in solid state lasers* (IntechOpen, 2010).

[31] J. L. Krause, K. J. Schafer, and K. C. Kulander, "High-Order Harmonic Generation from Atoms and Ions in the High Intensity Regime", Physical Review Letters **68**, 24 (1992).

[32] C. M. Heyl, C. L. Arnold, A. Couairon, and A. L'Huillier, "Introduction to macroscopic power scaling principles for high-order harmonic generation", Journal of Physics B: Atomic, Molecular and Optical Physics **50**, 013001 (2016).

[33] R. Paschotta, *Gouy Phase Shift [online]*, `https://www.rp-photonics.com/gouy_phase_shift.html`, (visited on 23/03/2023).

[34] P. Balcou, P. Salières, A. L'Huillier, and M. Lewenstein, "Generalized phase-matching conditions for high harmonics: the role of field-gradient forces", Phys. Rev. A **55**, 3204–3210 (1997).

[35] C. M. Heyl, J. Güdde, A. L'Huillier, and U. Höfer, "High-order harmonic generation with μj laser pulses at high repetition rates", Journal of Physics B: Atomic, Molecular and Optical Physics **45**, 074020 (2012).

[36] C. G. Durfee, A. R. Rundquist, S. Backus, C. Herne, M. M. Murnane, and H. C. Kapteyn, "Phase matching of high-order harmonics in hollow waveguides", Phys. Rev. Lett. **83**, 2187–2190 (1999).

[37] E. Constant, D. Garzella, P. Breger, E. Mével, C. Dorrer, C. Le Blanc, F. Salin, and P. Agostini, "Optimizing high harmonic generation in absorbing gases: model and experiment", Phys. Rev. Lett. **82**, 1668–1671 (1999).

[38] G. Porat, C. M. Heyl, S. B. Schoun, C. Benko, N. Dörre, K. L. Corwin, and J. Ye, "Phase-matched extreme-ultraviolet frequency-comb generation", Nature Photonics **12**, 387–391 (2018).

[39] T. K. Allison, A. Cingöz, D. C. Yost, and J. Ye, "Extreme nonlinear optics in a femtosecond enhancement cavity", `10.1103/PhysRevLett.107.183903` (2011).

[40] A. Becker, N. Aközbek, K. Vijayalakshmi, E. Oral, C. M. Bowden, and S. L. Chin, "Intensity clamping and re-focusing of intense femtosecond laser pulses in nitrogen molecular gas", Applied Physics B: Lasers and Optics **73**, 287–290 (2001).

[41] T. Popmintchev, M.-C. Chen, A. Bahabad, M. Gerrity, P. Sidorenko, O. Cohen, I. P. Christov, M. M. Murnane, and H. C. Kapteyn, "Phase matching of high harmonic generation in the soft and hard x-ray regions of the spectrum", Proceedings of the National Academy of Sciences **106**, 10516–10521 (2009).

[42] J. Rothhardt, M. Krebs, S. Hädrich, S. Demmler, J. Limpert, and A. Tünnermann, "Absorption-limited and phase-matched high harmonic generation in the tight focusing regime", New Journal of Physics **16**, 033022 (2014).

[43] M. V. Ammosov, N. 8. Delone, and V. P. Krainov, "Tunnel ionization of complex atoms and of atomic ions in an alternating electromagnetic field", Sov. Phys. JETP **64**, 1191–1194 (1986).

[44] W. Umrath, R. Bahnen, T. Dreifert, H.-U. Haefner, R. Hölzer, F. Kadi, E. Mossolff, H. Litterscheid, R. Rey, H. Rottländer, W. Scheer, F. Schönborn, and G. Voß, "Grundlagen der Vakuumtechnik", (2016).

[45] É. Clapeyron, "Mémoire sur la puissance motrice de la chaleur", Journal de l'École Polytechnique, 153–190 (1835).

[46] W. Demtröder, *Mechanics and thermodynamics* (2017), pp. 299–301.

[47] *Non-ideal gas - Van der Waal's Equation and Constants. [online]*, (2017) `https://www.engineeringtoolbox.com/non-ideal-gas-van-der-Waals-equation-constants-gas-law-d_1969.html` (visited on 02/01/2023).

[48] J. Nauta, J.-H. Oelmann, R. Pappenberger, P. Knauer, J. Krummeich, N. Lackmann, H. Ledwa, I. S. Muhammad, J. Stark, T. Pfeifer, and J. R. Crespo López-Urrutia, "A low-vibration, differentially pumped vacuum system for intra-cavity high-harmonic generation", (In preperation).

[49] J. Hollenshead and L. Klebanoff, "Modeling radiation-induced carbon contamination of extreme ultraviolet optics", Journal of Vacuum Science and Technology B: Microelectronics and Nanometer Structures **24**, 64 (2006).

[50] R. Pappenberger, "Implementierung eines differentiellen Pumpsystems zur Erzeugung eines ultravioletten Frequenzkamms in einem optischen Resonator" (Ruprecht-Karls-Universität Heidelberg, 2019).

[51] P. E. Miller and M. B. Denton, "The quadrupole mass filter: basic operating concepts", Journal of Chemical Education **63**, 617–622 (1986).

[52] *Quadrupol-Massenfilter [online]*, `https://www.pfeiffer-vacuum.com/de/know-how/massenspektrometer-und-restgasanalyse/quadrupol-massenspektrometer-qms/quadrupol-massenfilter/` (visited on 11/03/2023).

Acknowledgements

Als ich mich in meinem dritten Semester nach einem Praktikum umschaute bin ich zufälligerweise in der EBIT Gruppe gelandet. Schnell wurde ich überzeugt von Josés enthusiastischer Führung durch das Labor und der warmen Arbeitsgruppenatmosphäre. José, vielen Dank für die Möglichkeit meine Bachelorarbeit in dieser Gruppe anzufertigen und das stets offene Ohr.

Herzlichen Dank an Thomas Pfeifer für das Übernehmen der Zweitkorrektur.

Ein ganz großes Dankeschön geht an Lennart. Du hast dir unglaublich viel Zeit genommen für meine Betreuung. Am Wochenende standest du im Labor und hast das Gas Recycling System aufgefüllt, auf abendteuerliche Art und Weise wurde das Volumen der Membranpumpe bestimmt und keine Frage blieb unbeantwortet. Ich konnte sehr viel von dir lernen. Vielen Dank! Danke an Jan-Hendrik. Auch du hast dir sehr viel Zeit genommen und mir bei Problemen immer zur Seite gestanden. Deine Begeisterung für das Experiment war sehr ansteckend. Tobias, deine Programmierfähigkeiten sind bewundernswert. Vielen Dank für das Beantworten zahlreicher Fragen!

Danke an den Rest des XUV-Teams, der EBIT-Gruppe und an das Studentenbüro. Ich hatte eine unvergessliche Zeit und bin euch sehr dankbar für all die schönen Mittagspausen, sowie Abende, die wir gemeinsam lachend verbracht haben.

Außerdem möchte ich mich bei all meinen Freunden, insbesondere Sara, Luise, Franziska und Simon W., für die Unterstützung und die schönen Jahre bedanken. Simon W., Simon A. und Luise, vielen Dank für das Korrekturlesen meiner Arbeit.

Schlussendlich möchte ich mich bei meinen Eltern und meinen Geschwistern herzlich bedanken. Ohne euch wäre ein Studium in Heidelberg undenkbar gewesen. Danke für eure konstante Unterstützung in jeglicher Hinsicht!